# The Arce Tephra: two subsequent paroxysmal Plinian eruptions from Coatepeque Caldera (El Salvador)

S. Kutterolf[1], J.C. Schindlbeck-Belo[2], I. Rohr[1], M. Rademacher[1], A. Cisneros de León[2], S. Eisele[3], A. Freundt[1], W. Hernandez[4], K.-L. Wang[5,6]

[1] GEOMAR Helmholtz Centre for Ocean Research Kiel, 24148 Kiel, Germany

[2] Institute of Earth Science, University of Heidelberg, Im Neuenheimer Feld 234-236, 69120 Heidelberg

[3] Asian School of the Environment, Nanyang Technological University, Singapore

[4] Observatorio Ambiental, Ministerio de Medio Ambiente y Recursos Naturales (MARN), San Salvador, El Salvador

[5] Institute of Earth Sciences, Academia Sinica, Taipei 11529, Taiwan

[6] Department of Geosciences, National Taiwan University, Taipei, Taiwan

Corresponding author: Steffen Kutterolf, skutterolf@geomar.de

## Abstract

The Coatepeque volcanic complex in El Salvador produced at least four Plinian eruptions within the last 80 kyr. The eruption of the 72 ka old Arce Tephra formed the Coatepeque Caldera and was one of the most powerful explosive eruptions in El Salvador. Hitherto it was thought that the Arce tephra had been emplaced only by one, mostly Plinian, eruptive event that ended with the deposition of a thick ignimbrite.

However, our stratigraphic, geochemical, and zircon data reveal a temporally closely-spaced double eruption separated by a gap of only a couple of hundred years, and we therefore distinguish Lower and Upper Arce Tephras. Both eruptions produced in the beginning a series of fallout units generated from fluctuating eruption columns and turning wind directions. The final phase of the Upper Arce eruption produced surge deposits by several eruption column collapses before the terminal phase of catastrophic ignimbrite eruption and caldera collapse. Mapping of the individual tephra units including the occurrences of distal marine and lacustrine ash layers in the Pacific Ocean, the Guatemalan lowlands and the Caribbean Sea, result in 25.6 km$^3$ tephra volume, areal distribution of 4x10$^5$ km$^2$ and eruption column heights between 20 - 33 km for the Lower Arce eruption, and 40.5 km$^3$ tephra volume, including 10 km$^3$ for the ignimbrite, distributed across 6x10$^5$ km$^2$ and eruption column heights of 23-28 km for the Upper Arce eruption. These values and the detailed eruptive sequence emphasize the great hazard potential of possible future highly explosive eruptions at Coatepeque Caldera, especially for this kind of double eruption.

**Keywords:** Central American Volcanic Arc, El Salvador, Coatepeque, Plinian volcanism

## 1 Introduction

The Coatepeque Caldera system in northern El Salvador generated at least four large explosive eruptions in the last 80 kyr (Kutterolf et al. 2008a), which produced the Bellavista Tephra (77 ka), the Arce Tephra (72 ka), the Congo Tephra (53 ka) and the Conacaste Tephra (51 ka). Because of their proximity to the active volcanoes almost all El Salvadorian cities are highly vulnerable to such highly explosive eruptions. It is therefore indispensable to analyze past eruptions with respect to eruption regime, eruption parameters and consequences for the surrounding area to better assess the hazards of future eruptions.

Here we focus on the Arce Tephra, first described in the geothermal report from CEL (1992), which was deposited ~72 ka ago by a caldera-forming eruption (Rose et al. 1999). It is characterized by an inverse graded pumice deposit, which is rich in biotite and shows banded pumice clasts as evidence for magma mixing (Kutterolf et al. 2008a). Reconnaissance mapping revealed a fall and flow sequence with a minimum distribution area of 2,000 km$^2$ and a tephra volume of 40 km$^3$ (CEL, 1992). Kutterolf et al. (2008a) compositionally correlated marine ash layers in gravity cores offshore El Salvador and Guatemala with the Arce Tephra. The Arce Tephra has not previously been studied in detail. However, distal deposits in El Salvador, the Pacific Ocean, the Guatemalan lowlands and the Caribbean have been identified by Kutterolf et al., (2008a, 2016) and suggest a much larger tephra volume than previously thought. Moreover, overview stratigraphic investigation of medial outcrops and discrepancies in first chemical analyses observed by Kitamura (2017) indicated that the eruptive and magmatic history may be complex and therefore a matter of interest for further research.

Kutterolf et al. (2016) correlated two ash layers that are separated by a few centimeters of lacustrine sedimentation in the ICDP (International Continental Drilling Program) drill cores of Lake Petén Itza in the Guatemalan lowlands with the Arce Tephra. The two layers were subdivided into Lower and Upper Arce Tephra but correlation with proximal localities has not been documented. In 2013, we therefore revisited the Arce Tephra in northern El Salvador to 1) record stratigraphic changes in detail, 2) map the distribution of the resulting units, and 3) sample the different tephra units for correlation purposes and to decipher compositional variations within the eruption (Fig. 1). The ultimate goal was to present a complete and detailed stratigraphy of the Arce Tephra in order to reconstruct the eruption sequence and quantify the eruption parameters. Our study confirms the subdivision of the Arce Tephra into Lower and Upper Arce Tephra as suggested by Kutterolf et al. (2016), which extends the eruption record of the Coatepeque Caldera from four to five Plinian eruptions within the last 80 kyr. Petrogenetic relationships between the two Arce units and the other Coatepeque Tephras will be presented elsewhere.

## 1.1 Geological setting

The volcanic front of El Salvador is part of the Central American Volcanic Arc (CAVA). Its volcanic activity along the western coast of Central America is driven by the subduction of the

Cocos Plate underneath the Caribbean Plate along the Middle American trench with velocities of 73 to 92 mm/year (DeMets, 2001). The recent volcanic front of El Salvador runs almost parallel to the coastline at a distance of 150–200 km from the trench and consists of 21 volcanoes that were active in the Holocene (Fig. 1). These produced many Plinian and sub-Plinian eruptions, some of which formed large calderas (Siebert et al., 2010).

A major E–W trending strike slip fault system (El Salvador Fault Zone=EFZ) developed due to the oblique subduction of the Cocos plate beneath the Caribbean plate along the volcanic front (Martínez-Díaz et al., 2004). From geological and seismological analyses it is interpreted that this dextral transcurrent component has caused segmentation of the arc and formation of major pull-apart structures that link the three larger segments of the EFZ (Agostini et al 2006).

The Coatepeque Caldera is located in the northern-most pull-apart basin, which reflects the extensional regime extending between the cities of Santa Ana and San Salvador. It is one of the largest calderas in El Salvador (6.8 x 5.6 km) and located at the southernmost end of the Guatemalan highlands (Rose et al., 1999) (Fig. 1). In the last 80 kyr the Coatepeque volcano produced several potassium-rich rhyolitic Plinian eruptions; the Bellavista Tephra, the Arce Tephras, Congo Tephra and Conacaste Tephra (Kutterolf et al., 2008a, Rose et al., 1999, Kutterolf et al., 2016), with the Arce units building the thickest proximal and medial fall and flow deposits in this region, uniquely characterized by its high biotite content.

## 2 Methods

### *Tephra distribution and volumes*

In order to establish stratigraphic relations and lateral and vertical variations in the Arce Tephra and construct isopach and isopleth maps of units (Fig. 1, Supplementary Table 1), we studied 46 outcrops in a clockwise semi-circle from NW through N to SE of Coatepeque caldera, extending from the caldera rim to about 30 km radial distance. Unfortunately, there are no outcrops of Arce Tephra in the E-W striking wide valley south of the caldera (Fig. 1). We studied distal ash deposits preserved in marine sediment cores in the Pacific Ocean (Schindlbeck et al., 2018; Kutterolf et al., 2008a) and the Caribbean (Rabek et al., 1985), and in lacustrine sediments of Guatemalan Lake Péten Itzá (Kutterolf et al., 2016).

Based on depositional structures and textures of pumices of individual beds, relative stratigraphic positions, lithic and mineral contents as well as the juvenile glass compositions, we subdivided the Arce Tephra into 10 stratigraphic units (I to X), correlated them between the outcrops and finally compiled a composite overview section for the entire Arce Tephra (Fig. 2). Crystal contents are visual percentage estimates made in the field that are cross-checked by inspecting crushed pumice material under the binocular. Units I to V compose the Lower Arce Tephra (LACT), and Units VI to X the Upper Arce Tephra (UACT) , the distinction being made on the basis of glass compositions and an incipient paleosol at the top of unit V (Fig. 2). Geochemical analyses are used for both stratigraphic correlations and petrogenetic interpretation. Selected detailed stratigraphic columns of complex tephra successions are shown in Figure S1. Thin sections from selected pumice clasts of every unit were acquired for petrographic analysis.

Subsequently, we compiled isopach maps for all 10 stratigraphic units. The tephra volumes were calculated by fitting straight lines to data on plots of ln (isopach thickness) versus square root (isopach area) following Pyle (1989) and Fierstein and Nathenson (1992) and integrating to infinity. Only when considering also the most distal outcrops the data required two straight-line segments to fit proximal to medial and distal data separately, where the point of intersection of these line segments also defines the boundary between the respective proximal to medial and distal facies.

Conversion of magma volume into dense rock equivalent magma mass (DRE), including volume correction factors for the interparticle pore space, lithic contents and ash dispersed in marine sediments, was done following Kutterolf et al. (2007, 2008b) using measured bulk pumice, ignimbrite and marine ash densities given therein.

### *Whole-rock analysis*

Whole-rock chemical analysis were conducted on glass pellets from pulverized juvenile pumice lapilli using an automated Philips X'Unique PW 1480 X-ray fluorescence analyser (XRF) at IFM-GEOMAR in Kiel. Precision for most elements was <0.1 wt.% for major and <10 ppm for most trace elements. Trace elements were analyzed with inductively coupled plasma mass spectrometry (ICP-MS) at the University of Kiel, using a Quadrupol-mass spectrometer (Agilent 7500cs, VG PlasmaQuad 1) and following the procedure of Garbe-Schönberg (1993).

### *Electron microprobe*

Glass compositions of crushed and wet-sieved juvenile pumice clasts were analyzed for major and minor element concentrations with a JEOL JXA 8200 wavelength dispersive electron microprobe (EMP) at GEOMAR, Kiel. In total we performed 2400 single glass shard analyses for 170 samples and subsamples. We analyzed fifteen single glass shard measurements per sample. Measurement conditions at the EMP follow Kutterolf et al. (2011) and include programs calibrated with international natural and synthetic standards. The glass analyses were performed using a measurement program for felsic glass at a constant voltage of 15 kV, a beam current of 6 nA and a beam size defocused to 5µm to overcome eventual Na-loss. The counting time for the signal was 20 s and 10 s for the background for major elements, 30 s and 15 s for minor elements.

Glass analysis experienced standard deviations of <1% for the major elements ($SiO_2$, $Al_2O_3$,) and < 10% for minor elements ($FeO_t$, MgO, CaO, $K_2O$, $Na_2O$, $TiO_2$) regarding glass analysis. Only for $MnO_2$ and $P_2O_5$ the deviations are larger than 20%. Glass compositions and errors are presented in Supplementary Tables 2 and 3.

### *LA-ICP-MS*

Trace element concentrations of 32 glass shards were determined by Laser Ablation Inductively Coupled Plasma - Mass Spectrometry (LA-ICP-MS) at the at the Institute of Earth Science at the Academia Sinica in Taipei (Taiwan) in 2016. A Photon Machines Analyte G2 laser ablation system using a 193 nm ArF Excimer laser was set to a spot size of 16 to 30 μm using 5-10 J/cm$^2$ energy density at 1-5 Hz repetition rate and coupled to a magnetic sector ThermoFinnigan Element XR ICP-MS mass spectrometer. Additionally 9 glass shards from three units (II, III, IV) were re-measured with LA-ICP-MS at GEOMAR, using a double-focusing, magnetic sector mass spectrometer (Nu-Instruments, AttoM), which is coupled to a 193 nm Excimer laser ablation system (Coherent, GeoLasPro). International standard glass (BCR-2g) were measured between sample measurements to monitor accuracy and correct for matrix effects and signal drift in the ICPMS as well as for differences in the ablation efficiency between the sample and the reference material (Günther et al., 1999). Concentrations of NIST reference material SRM 612 (Taiwan) and SRM610 (GEOMAR) were used for external calibration. In both facilities silica and calcium concentrations, measured by EMP, were used also as internal standards to calibrate the trace element analyses. For detailed measurement conditions see Stoppa et al. (2018) and Schindlbeck et al. (2018).

The limit of detection (LOD) for most trace elements is generally not greater than 100 ppb. For REEs, the LOD is generally around 10 ppb. The analytical precision was generally better than 10% for most trace elements and the comparative measurements of the same samples in both labs show very good agreement (within natural sample deviation from mean, and difference between lab measurements, are mostly <6% for all measured elements). Trace element compositions including standards and errors are given in Supplementary Tables 3 and 4. The new analyses complement 9 glass shard measurements given by Kutterolf et al. (2008a).

### *U-Th zircon crystallization ages*

In order to separate zircon crystals from composite pumice samples of Lower and Upper Arce eruptions, pumice blocks were crushed and sieved to □200 µm fractions. Heavy minerals were concentrated by standard heavy mineral separation techniques that included washing and hydraulic panning. Zircon crystals were hand-picked with the help of a binocular microscope. In order to dissolve glass attached to zircon, crystals were treated for 5 minutes with cold 40% HF. Glass-free crystals were pressed into indium (In) metal which allowed to analyze the outmost crystal faces, and thus the youngest crystallization event. Prior to analysis, the mounts were gold coated.

Zircon U-Th dating was conducted on a CAMECA ims 1280-HR ion microprobe at the Institute of Earth Sciences at Heidelberg University, Germany. $^{238}$U-$^{232}$Th-$^{230}$Th isotopes in zircon were measured following analysis protocols described in Reid et al. (1997) with modifications according to Schmitt (2011). A mass-filtered $^{16}O^{-}$ primary ion beam with an intensity of 35-45 nA was focused to a spot of 30-35 μm. Secondary ions were accelerated at 10 keV with an energy bandpass of 50 eV and a mass resolving power ($m/m\Delta$) of 6000. Due to higher secondary ion yields for actinide oxides over atomic species (Schmitt, 2011; Schmitt and Vazquez, 2017), intensities of $^{230}ThO^{+}$, $^{232}ThO^{+}$ and $^{238}UO^{+}$ and reference species $^{90}Zr_2O_4^{+}$ were measured. Simultaneous detection of $^{230}ThO^{+}$ and $^{232}ThO^{+}$ was achieved using electron-multiplier (EM) and Faraday cup (FC) detectors in order to reduce the analysis time up to ~30% compared to mono-collection analysis. Gains for both detectors were calibrated by measuring $^{180}HfO^{+}$ in both detectors at the beginning of the session; no significant drift was found throughout the session. $^{230}ThO^{+}$ intensities were corrected by subtracting the averaged intensities measured during each analysis on two mass fixed stations at 244.03 and 246.3 amu. The U-Th relative sensitivity factor (RSF) was calibrated based on secular equilibrium reference zircon AS3 ($^{206}$Pb/$^{238}$U age = 1099 Ma; Schmitz et al., 2003). Interspersed analyses of the same reference zircon yielded a weighted mean value for the analytical session of ($^{230}$Th)/($^{238}$U) = 1.027 ± 0.005 (1σ; mean square of weighted deviates MSWD = 0.83; number of spots n = 26). Zircon isochron ages and initial ($^{230}$Th)/($^{232}$Th) were calculated by fitting data for the unknowns with an error weighted linear regression using Isoplot 4.1 (Ludwig, 2003). In addition U-Th model ages from two-point isochrons defined by the U-Th zircon activity ratio and that of upper continental crust U-Th (Rudnick and Fountain, 1995) assuming secular equilibrium.

## 3 The Lower and Upper Arce Tephras

We distinguish ten stratigraphic units in the Arce Tephra succession that differ in their sedimentological appearance, mineralogy and glass composition (Fig. 2). Units I to V compose the Lower Arce Tephra (LACT), and Units VI to X the Upper Arce Tephra (UACT), which are separated by a layer boundary affected by erosion on which an incipient paleosol was initiated. Although some outcrops contain nearly all units, a master outcrop containing all ten units has not been found and we therefore correlated and combined 46 outcrops from proximal (0.5 km from vent) to medial (up to 30 km from the vent) distance for a composite stratigraphic succession (Figs. 1, 2). Field-based unit correlations between the different outcrops are verified by the compositional variations of the juvenile components (minerals, pumices, matrix ash). In the following, the term “fall” layers is used for deposits that are characterized by mantle bedding and relatively good grain-size sorting in contrast to “flow” deposits that show poor sorting and signs of parallel and cross bedding as well as topography-controlled thickness changes.

In all proximal to medial units the Arce Tephra is predominantly composed of compositionally similar pumices (supplementary table 4) that appear in different colors due to textural differences obtained during ascent and eruption (e.g. compaction grade of pumice, strain features during ascent in the vent, and bubble content and texture). Subangular to angular pumice lapilli appearing silvery (~30 vol%) or white (~65 vol%) predominate over minor light-gray angular pumice lapilli (~5 vol%), all of rhyolitic composition (Fig. 3). Rare varieties of pumice lapilli include beige clasts or occasionally reddish-dark gray andesitic pumice clasts or white to light-gray banded pumice clasts (<1%). All pumice types are highly-vesicular and the silvery and white clasts are characterized by strongly elongated to tubular and parallel-oriented vesicles. The rhyolithic pumices contain biotite, feldspar (plagioclase and sanidine) and amphibole as isolated phenocrysts as well as crystal clusters. Plagioclase ($An_{18–50}$) range from albite to orthoclase and is the most abundant phenocryst phase, forming 5% of the entire sample including vesicles. Additionally, 1 to 3 vol% amphiboles, especially in the white angular clasts, as well as biotite up to 4 vol%, and pyroxene and sanidine with minor abundance can be found in the mineral assemblage. Very rare olivine can additionally be observed in the dark gray pumice clasts. The phenocryst phases also occur as free crystals in the ash fraction of the tephra, with proportions varying with stratigraphic position. The biotite content of pumice clasts is the main criterion for distinction between Arce deposits and other tephras in this region. Below we will describe briefly the characteristic stratigraphic and compositional features of all units, how they can be correlated with each other, and how they change or vanish from proximal to distal outcrops. The detailed descriptions of these successions are given in the online supplementary (Fig. S1).

Tephra correlation is based largely upon major and trace element geochemical analyses of glass shards from each stratigraphic tephra unit, but major and trace element analyses of bulk samples are also compared here. All data, despite one trachytic and one trachyandesitic sample, fall into the rhyolite field of the total alkali versus silica (TAS; Fig.3) classification after Le Maitre et al. (2002). Glass compositional of the Arce Tephra also differ from those of other Coatepeque tephras in the TAS diagram (Fig. 3). The Arce samples form two chemical groups. Group A has higher alkali (9.4 – 10 wt%) but lower silica contents (70.5 – 73 wt%) compared to group B with relatively higher silica (74.8 – 77.6 wt%) and lower total alkali contents (9.3 – 8.5 wt%). Group B compositions overlap with Bella Vista Tephra glass data (Figs. 3, 4). Samples from Lower Arce units can be found in both geochemical groups, whereas samples from the Upper

Arce Tephra only occur in group B (except the ignimbrite in Unit X see below). This discrimination is assisted by an $FeO_t$ and $Na_2O$ versus $SiO_2$, and $K_2O$ versus CaO diagram (Fig. 4A, B, C), where group A contains much higher FeOt, $Na_2O$, and CaO concentrations (0.9 – 1.3 wt%) than group B at similar high $K_2O$ contents (4.8 – 5.3 wt%), and higher $SiO_2$ concentrations, overlapping with Bella Vista glass data again. Arce bulk rock compositions have generally lower alkali contents (8.3 – 9.2 wt%) but similar silica concentrations compared to group A glasses (70.5 – 74.5 wt%) (Fig. 3). It is noteworthy that glass shard compositions and group affiliation do not correlate with pumice color and texture.

The compositional differences between groups can also be observed in the trace element data and are best exemplified in the Ba/La versus Rb/Hf, and Ba/Zr versus La/Sm diagram. Group A has high Ba/La and Ba/Zr ratios at lower Rb/Hf and Zr/Nb values whereas group B shows contrary behavior in these element ratios (Fig. 4 D, E, G). However, in contrast to the major elements, group B trace elements compositions do not overlap with those of Bella Vista Tephra.

## *3.1 Lithology, composition and stratigraphy of the Arce succession*

### *Lower Arce Tephra*

#### *Unit I*

Unit I is found in in medial to distal areas (circa 10 to 20 km, e.g. outcrops A1 and A23; Fig. 1) from the vent. Unit I is a ~3 to 35 cm thick, massive, and well-sorted lapilli layer that contains white, silvery-white and light-gray pumice clasts in more proximal outcrops (e.g., A1; Figs. 2, 5, 6D, G, 7A, Supplement Fig. 1). It overlies an older brownish tuff in sharp contact. In the most proximal outcrop A3 (ca. 4 km East of Coatepeque caldera rim) the layer is 80 cm thick, shows an inverse grading from coarse ash to medium sized pumice lapilli and faint stratification, characterized by multiple small-scaled grain size changes including also horizons with increased lithic contents (up to 20 vol%) (Figs. 5, 6G). Lithic components are fresh and hydrothermally altered lava clasts, but are rare in medial and distal outcrops (<5 vol%). Crystal contents in the pumice lapilli and matrix are between 5 vol% in medial to 10 vol% in more proximal outcrops and have a phenocryst assemblage of biotite (bt) > feldspar (fsp) > amphibole (amph) that is typical for the Arce Tephra that includes. In outcrops A6 (1-2 mm thickness) and A23 (3 cm thickness) thickness of Unit I is reduced to a crystal-rich basal ash directly on the contact to the underlying paleosol.

Glass shard compositions correspond to geochemical group B with low CaO, $FeO_{tot}$, and $SiO_2$ (Figs. 3, 4C). This is consistent with low Ba/La and Ba/Zr values within white pumices indicative of group B.

The boundary from Unit I to Unit II is often vague and mostly characterized by a grain size increase and the appearance of gray pumice clasts of trachytic composition in Unit II (Figs. 3, 6D, G, Supplementary Fig.1).

### *Unit II*

Unit II is a package of two massive, well-sorted fallout beds (e.g., outcrop A39) of fine and medium pumice lapilli (Figs. 2, 5)that are normal graded in their uppermost part. Thicknesses vary between ~12 cm to ~ 125 cm in total (distal to proximal, respectively). Pumice clasts are generally angular, white, silvery white and gray lapilli. The lowermost part is characterized by fine to medium, white (2/3) and gray (1/3), pumice lapilli. At medial distances the first lapilli bed shows a continuous upward decrease of grain size from medium lapilli to coarse ash in the first third of the unit followed by a sudden increase, up to coarse lapilli, at the onset of the second lapilli bed. The second bed is also normally graded at the top (Figs. 5, Supplementary Fig.1). In the most proximal outcrops (A3, A43) clear layering at cm to dm scale can be observed in the lower part, equivalent to the lower bed in medial outcrops, showing individual well-sorted and well-delimited beds of fine and/or medium lapilli but also fine and/or coarse ash (outcrops A3, A43; Figs. 6D,G, 7A). The upper bed shows a grain size decrease in the upper part, is massive in medial outcrops, and has only faint bedding marked by alignments of larger clasts in the proximal outcrops (Fig. 6D).

The lower bed contains 10 vol% phenocrysts (matrix and pumice) and 10 vol% lithics (fresh lava clasts) as well as some gray and banded pumices. The upper bed consists mainly of crystal-poor white pumices (5-10 vol%), 10-15 vol% crystals (bt >amph>fsp) in the ash and also 10-15 vol% of predominantly hydrothermally altered lithics. The phenocrysts generally occur with sizes of up to 0.5 cm in the most proximal outcrops in both, the pumices and the matrix. In the medial to distal outcrops west of Coatepeque caldera (outcrop A6; Fig. 1), the upper part (11 cm) of the unit is normally graded from medium pumice lapilli to fine lapilli and therefore a more distinct boundary to subsequent Unit III (Fig. 7A). To the southeast and east (outcrops A10, A23, A39, Fig. 1) the unit is only vaguely normal graded.

Glass shard major and trace element compositions are distributed across both geochemical groups (Figs. 3, 4A-E). Unit II therefore shows a mixture of group A and B compositions. Exceptions are the gray pumices, which have a unique, trachytic composition (5.5 wt% $Na_2O$, 3 wt% $K_2O$, 5.7 wt% $FeO_t$, 64.2 wt% $SiO_2$, 3.7% CaO, 16 wt% $Al_2O_3$).

At the boundary between Units II and III grain size increases strongly up to block size pumice clasts in the most proximal locations (e.g., outcrops A23, A4, A3), coinciding with the occurrence of a horizon enriched (~15-20 vol%) in predominantly hydrothermal altered lithics at the base of Unit III, best observed to the east of the caldera (outcrops A3, A23).

### *Unit III*

Unit III is a massive, and well to moderately sorted pumice lapilli deposit in medial to proximal sections, with thicknesses from 1 m to at least 4 m (e.g., outcrops A1, A23; Figs. 1, 2, 5, 6C, D, 7A, B, Supplementary Fig.1). It shows a normal grading at the top (in more distal outcrops over the entire unit) from fine lapilli to ash (e.g., outcrops A10, A39).

Unit III consists predominantly of angular, silvery-white, and white pumice clasts often with included lithic clasts, and also some gray, olivine bearing pumices, especially in the lower part of the most proximal outcrops (e.g., A3, A43). Lithic content, besides the lithic-rich base, is poor (5 vol%) in medial and distal outcrops but can be moderate up to 10 vol% in more proximal locations and comprises mostly fresh andesitic lava fragments. Unit III pumice lapilli have a phenocryst content of 10 vol% with feldspar as the major mineral phase and abundant biotite and common amphibole; occasionally olivine occurs surrounded by the trachytic/trachyandesitic matrix. Amphibole-dominated cumulates occur in proximal outcrops (A30, A23, A2 and A26).

Glass shard compositions from Unit III are typically within geochemical group A, with high CaO, Ba/La and Ba/Zr values (Fig. 3, 4A-E).

The Unit III to IV boundary is marked first by an increase in grain size and lithic content before both are decreasing again. Therefore, this change is difficult to recognize in some outcrops. This is especially true in the eastern, northeastern and southeastern region of the caldera (outcrops A21, A23, A39; Fig. 5) where there is a continuous decrease in grain size from Unit III to IV.

### *Unit IV*

In medial and distal areas Unit IV is well-sorted, massive to vaguely stratified with thicknesses between 5-20 cm (e.g., outcrops A6, A31; Figs. 1, 2, 5, 7A, B to E, Supplementary Fig.1). This unit is exclusively exposed in the northwest of the caldera. After a short interval of increasing grain sizes at the base (fine to medium lapilli) the unit is normally graded up to fine ash at the top. Pumice clasts are exclusively white with moderate crystal contents (10-15 vol%). Thickness increases up to 55 cm in more proximal outcrops (e.g., outcrop A1; Fig.5). Lithic contents are poor to moderate (5 to 10 vol%) and comprise hydrothermally altered and fresh lava fragments. Exceptions are the basal cm-thick horizon in medial outcrops where lithic contents can be as high as 40 vol%, and the uppermost 20 cm of Unit IV where they increase again up to 20 vol% (e.g., outcrop A23). Overall crystal contents in the matrix range around 10-20 vol% (bt>fsp>amph).

Glass shard compositions of Unit IV are exclusively within geochemical group B (Fig. 3, 4). This contrasts with the group A glass compositions of Unit III and thus justifies the stratigraphic subdivision although the boundary is not well defined in the field. The transition into Unit V is gradational and marked by a further decrease in grains size.

### *Unit V*

Unit V is a very prominent, sometimes two-partite white and occasionally pinkish to beige/brown, up to 20 cm thick layer of fine ash. In the outcrops to the west of the caldera (outrcops A8, A6; Figs. 1, 2, 5, 7A to E, Supplementary Fig.1) it is characterized by a uniform ash layer that shows normal grading from coarse ash to fine ash, which appears to be a continuation of Unit IV. The ash layer is often cut by irregular and wavy erosional channels (mm to also m-scale) that are filled by the overlying fallout (Unit VI; e.g., outcrop A8; Figs. 7A,D, Supplementary Fig.1). Apart from the erosion, Unit V thickness remains constant at outcrop scales. The topmost mm are locally brownish altered.

In the outcrops to the north and to the east of the caldera, Unit V commonly forms a double layer (Fig. 7C,E). The lower layer, several cm thick, is laterally continuous, well-sorted fine white ash that is similar to Unit V in the west. The overlying pinkish to beige, fine to coarse ash with some rounded fine lapilli shows lateral thickness variations (2-10 cm) and occasionally faint lamination. The beige ash shows cross-bedding and contains rare mm-sized accretionary lapilli in outcrops A6 and A31. In outcrop A21 the basal contact of the beige ash shows mm-scaled ripples. In some outcrops the top of the beige ash has been partly eroded and/or an initial incipient soil started to form (e.g., outcrop A21; Fig. 7C) showing rare fine paleo-root veins that also cross into the underlying white ash.

Fine-grained feldspar, biotite and amphibole crystals (10 – 15 vol%) but nearly no lithic fragments (<5 vol%) can be identified in the lower white ash. The upper pinkish ash contains 15 – 20 vol% phenocrysts (bt>amph>fsp) and up to 15 vol% mm-sized lithics. Analyzed glass shards of Unit V fall in both geochemical groups (Fig. 3, 4A—E).

Combination of stratigraphic (erosional surfaces, initial incipient soil) and geochemical features demonstrate a longer break in the eruption after Unit V and therefore lead to the division of Lower and Upper Arce, although each piece of evidence would not be stand-alone arguments for an interruption of the eruption.

### ***Upper Arce Tephra***

#### *Unit VI*

Unit VI has a thickness of 8–30 cm in distal to medial outcrops towards the Northwest and West (e.g., outcrops A2, A1, A6, A8, E066) and 30–50 cm in medial to proximal outcrops towards the North and East (e.g., outcrops A21, A4, A43, A23; Figs. 1, 2, 5, 6A, C, 7A to E, Supplementary Fig.1). Although sometimes vaguely stratified, Unit VI is an overall well-sorted and massive fall deposit of fine to medium pumice lapilli. Towards the West the fall layers are inversely graded from fine ash to fine or medium pumice lapilli and mantle the topography. In proximal outcrops to the North and East a mm-thick lithic-rich (~20 - 30 vol%) lamina can be observed at the base. The whole unit is predominantly composed of silvery and white pumice with 5 to 10 vol% crystal content. The lithic content (hydrothermally altered lava fragments) in the medial and distal outcrops is moderate to poor (~10 vol%). The crystal content in the matrix ash ranges between 10 to 15 vol% (bt>amph>fsp) in all outcrops.

Glass shard compositions of Unit VI belong to geochemical group B. They range between 75 – 76.8 wt% $SiO_2$, 8.75 – 9.2 wt% total alkalis, 4.9 – 5.4 wt% $K_2O$, 1-1.5 wt% $FeO_t$, 3.5 – 4.1

wt% $Na_2O$ and 0.6 – 0.75 wt% CaO (Figs. 3, 4A-C). Consistently the respective trace elements show only low Ba/La and Ba/Zr values distributed over the entire range of group B (Fig. 4D, E).

The boundary between Unit VI and VII is marked by a strong increase in grain size and lithic contents as well as the deposition of a thick massive pumice layer.

### *Unit VII*

In the proximal and medial area Unit VII is a prominent thick and massive, slightly reverse graded, well-sorted pumice fall that is normally graded in the uppermost part. It is 1 to ~1.6 m thick with coarse pumice and lithic lapilli up to block size in the North and East of the Coatepeque Caldera (e.g., outcrop A42; Figs. 1, 2, 5, 6 C, 7A, B, F to H, Supplementary Fig.1). In the medial to distal outcrops West of the caldera the unit still has a thickness between 45 cm (outcrop A33) and 98 cm (outcrop A6; Fig. 1). The pumices are commonly silvery white, with rare light-gray fine lapilli. Lithics (~10 vol%) are made predominantly out of fresh andesitic lava fragments. In medial and proximal locations the basal part is enriched in lithics (~20 vol%) and amphibole-rich cumulates. In the normal graded part at the top, fresh and hydrothermal altered lithics are enriched (> 20 vol%). Phenocryst contents are moderate (20 vol%) with bt, fsp>amph.

Unit VII contains only group B glass shards around 75 wt% silica and ~9.2 wt% total alkalis (Fig. 3). Respective minor and trace elements indicate also only group B (Fig. 4).

The boundary from the normal graded top of Unit VII to Unit VIII is sharp and marked by an increase in grain size (Fig. 7G) and by the occurrence of a poorly sorted, grayish to pinkish basal lapilli tuff of Unit VIII (Fig. 7F).

### *Unit VIII*

The massive to vaguely bedded pumice layer of Unit VIII is normal graded at the top. Unit VIII is exposed in nine of the mapped outcrops, elsewhere it is either totally (e.g., outcrop A23; Figs.

1, 2, 5, 6C, 7F to H) or partly eroded by subsequent pyroclastic flows (e.g., outcrops A6, A29; Figs. 1, 6) or has not been deposited at all. It has an overall thickness between 18 to ~80 cm (outcrops A27, A6, A8, A42, E31; Figs. 1, 5, Supplementary Fig.1).

The appearance of Unit VIII strongly depends on the geographic position. Closer to the caldera and to the North it is exposed as a package of several cm to decimeter thick well-sorted, massive, medium/fine pumice lapilli fall beds with subangular clasts and overall vaguely variable grain size changes (e.g., outcrops A21, A4, E031; Figs. 2, 5, 8H). In the North the uppermost two beds are normal graded from medium to very fine ash at the top and contain increased lithic contents (20 vol%) with more hydrothermal altered andesitic lava fragments. In the West of the caldera, Unit VIII starts with a wavy, 0.5 to 3 cm thick, poorly sorted, lithic-poor, pinkish-brownish fine to medium ash that contains white, rounded, fine pumice lapilli. The overlying, 26 to 38 cm thick, well sorted, vaguely stratified to massive, fine to medium lapilli fall out has poor lithic contents (< 5 vol%) and shows a normal grading toward coarse ash and increasing lithic content up to 20 vol% at the top. Here, subrounded pumice clasts show sometimes a beige ash coating (e.g., outcrop A8). Generally, the phenocryst content of both facies is 15 %vol in matrix ash and pumices, consisting of bt> fsp > amph.

Glass shard compositions of Unit VIII samples lie only in geochemical group B with a narrow range between 75 – 75.2 wt% $SiO_2$, ~9 wt% total alkalis, ~5.2 wt% $K_2O$, ~1.3 wt% $FeO_t$, ~3.8 wt% $Na_2O$ and ~0.7 wt% CaO (Figs. 3, 4). The respective trace elements fall uniquely into group B and show overall lower Rb/Hf values (33 - 36) than Unit VI (43 - 46).

### *Unit IX*

Unit IX is only locally exposed and best preserved in a narrow corridor toward the North of the Coatepeque Caldera (e.g., outcrop A21; Fig. 1). It is characterized by two sequences of wavy, poorly sorted, partly stratified fine to medium ash-rich beds, each overlain by a moderately to well-sorted massive coarse ash to lapilli bed (Figs. 2, 5, 7G,H). To the northeast this unit only has a thickness of ~20 cm (e.g., outcrops E031, A4, A43; Figs. 1, 5, Supplementary Fig.1).

Each of the two sequences starts with a triple-layered (several cm-thick) whitish to pinkish-brown to pinkish-gray ash that often contains isolated, rounded, fine to medium pumice lapilli. The poorly sorted ash beds either show wavy boundaries or faint stratification and/or variable lateral thicknesses. Accretionary lapilli can further be observed in the lower ash-rich parts of the unit in outcrops E031 and A21. The normally graded, several cm-thick, laterally continuous pumice-dominated beds on top of the triple-layered ash packages are partly lithic-rich (~25 vol%; hydrothermal altered and fresh) and always contain a significant portion of fine to medium ash. The fine to medium sized silvery-white pumice lapilli are a mixture of angular, subrounded or even rounded clasts. The beds contain up to 30 vol% minerals in the matrix ash with biotite as most abundant mineral and amphibole as well as feldspar in minor portions. Dominantly hydrothermally altered lithics are present with variable amounts (5–20 vol %) and continuously increase toward the top of the lapilli beds.

Glass shard compositions of samples from Unit IX cover a wide range of geochemical group B in the TAS diagram and range between 0.7–0.8 wt% CaO, 5.1–5.3 wt% $K_2O$, 1.3–1.5 wt% $FeO_t$, ~3.4–4.0 wt% $Na_2O$, 75.9–76.5 wt% $SiO_2$, and 31–51 Rb/Hf (Figs. 3, 4).

### *Unit X*

Unit X is a poorly-sorted, matrix-supported pyroclastic flow deposit composed of several pyroclastic flow units that vary strongly in their lithic, crystal and pumice clast contents (outcrop A13; Figs.1, 2, 5, 6E, F, S1). Pumice clasts incorporated in the flow units are silvery-white, light-gray, reddish-gray and white and have fine lapilli to block size. Unit X is best exposed in outcrop A23 (Fig. 1, 6B), 9 km east of the caldera, where it is exposed as one flow deposit of more than 10 m thickness above an erosional unconformity cutting deep into the underlying units. In outcrop A13, which is located ca. 13 km northeast of the caldera, a ~12 m thick sequence of at least seven pyroclastic flow units can be distinguished by pronounced lithic- or pumice-enrichments at the bottom or at the top of every flow (Figs. 1, 7I), as well as by the slight color changes of the ashy matrix (pinkish, gray, beige or yellow). Some flow units show internal stratification in the form of lithic enrichments or ash bands with dune structures. The uppermost flow deposit contains some amphibole-cumulates with fragments of Bella Vista obsidian. In outcrop A14 (Fig. 1) dark colored lapilli pipes where observed in the lowermost flow units (e.g., Figs. 5, 6E, F).

Major element glass compositions of Unit X pumice samples commonly fall into the geochemical group B, but a third of the analyzed samples also fall into the group A discrimination field (Figs. 3, 4). Glass shards from the ignimbrite matrix ash homogenously have group B compositions. This probably indicates a reworking of pumice lapilli from underlying units (III and/or V) of compositional group A during the eruption. Trace element compositions of pumices plot within geochemical group B.

### *3.2 Distal and very distal outcrops*

The two Arce tephras can also be traced in distal regions on land (outcrops A37 and A39) and in very distal marine and lacustrine sediments. In the lowlands of Guatemala, 350 km north of the Coatepeque Caldera, the Arce tephras were recovered within the lacustrine sediments of Lake Péten Itzá in two ICDP (International Continental Drilling Project) drill holes (Fig. 4, 6H, I; Kutterolf et al., 2016). Two ~2 and ~0.4 cm thick fine ash layers (Peten 1B-16H-2, 72.2-72.5 and 75.4-78 cm; Peten 6B-19E-2, 106.4-106.8 and 111-112.4 cm), that are separated by 3 to 4 cm of lacustrine sedimentation, were identified as the distal deposits of the Arce eruption (Kutterolf et al., 2016). Glass shard composition of the Lower Arce Tephra plot within compositional group A, whereas the Upper Arce Tephra plot in the field of group B.

Additionally, two successive dispersed cm-thick ash layers can be observed ~1000 km to the North of Coatepeque Caldera in Caribbean Sea sediment cores (Tr126/22-321 and 358; and probably K131-429 and 446, Rabek et al., 1985) featuring the same compositional similarities as the proximal Arce deposits. Furthermore, both Arce tephras were also recovered as 3 to 6 cm thick pinkish-white ash layers at four coring locations in the Pacific Ocean, 200–350 km Southwest of the Coatepeque Caldera (Meteor cruise sites M66-226, 229, 230 and DSDP Site 499; Kutterolf et al. 2008a; Schindlbeck et al., 2018) (Figs. 1, 4). Correlations match generally both Arce major and trace element field compositions, despite a loss in $K_20$ in the M66 marine samples (due to alteration), and are also assisted by trace elements. The marine Arce tephra at DSDP Site 499 and at sites M66-229 and M66-230 plot, in the compositional field of group B and may indicate an attribution to the Upper Arce Tephra, whereas the sample from site M66-226 contains glass shards from both geochemical groups and therefore can be defined as deposit from the Lower Arce Tephra. A genetic relation to either Plinian fall or co-ignimbrite ash like suggested by Kutterolf et al. (2016) cannot be confirmed by our much more detailed compositional and textural analysis.

## 4 Discussion

### *4.1 Facies interpretation and eruption(s) sequence*

Sedimentological and compositional changes of each unit were used in addition to obvious signs of pauses in the eruption to characterize the detailed stratigraphic succession and its related sequence of eruption phases. Proximal outcrops provide additional information about sectorial variations around the caldera. However, no accessible vertical sections are available in the sectors south of the caldera, so observation of lateral facies changes remained limited to the arc from west through north to east. Two of the studied sections are at most a few hundred meters away from the caldera rim, and depositional features diagnostic of specific transport processes had little time to develop before emplacement. Therefore, these proximal sedimentation areas around the vent can be affected by more than one eruption and emplacement process (e.g., Fierstein et al. 1997). A summary of the interpretations is given as a schematic eruption sequence in Figure 8. In the following we describe the eruption conditions for each of the ten units in detail.

The basal Unit I shows vague stratification and an overall steady upward increase in grain size, which indicates small explosions and an increase in eruption intensity during this initial phase. Stratification and multiple horizons that are enriched in lithics, especially in the proximal areas around the vents (outcrop A3) may indicate either several pulses of lateral explosions in a relatively low eruption column or just a very weak and oscillating eruption column. There is no evidence for an influence of external water during this first eruption phase. Which suggests that the precursory Bella Vista eruption had not yet formed a significant caldera in which water would have ponded.

Unit II is characterized by an increase in grain size, the appearance of gray pumice lapilli of trachytic composition as well as fresh and hydrothermally altered lithic fragments, which overall indicate an intensification of the eruption. The bedding and abrupt proximal grain size changes between single beds in the beginning suggests rather unstable eruption conditions that are getting more stable toward the upper part of Unit II. The appearance of the trachytic pumices suggests either the influx of new and less evolved magma that might have triggered the eruption, or higher magma discharge rates tapped deeper regions of the reservoir (cf. Blake and Ivey 1986) where the less evolved magma resided. In outcrops that are located in the northwestern part of the caldera, the grain size decreases towards the top of Unit II, which may be due to a weakening of the eruption and therefore decreasing eruption column or a change in wind direction and therefore the change in direction of the dispersal axis. Isopach maps of Units I to III all show similar dispersal directions (Figs. 9c and d) and therefore a change in wind direction at the end of Unit II is very unlikely.

A high, well-developed and stable eruption column is inferred for emplacement of the widespread, thick, well-sorted, massive and coarse pumice lapilli layer of Unit III. Lithic enrichment at the base of the unit may be interpreted as vent widening. Continuous weakening of the eruption column or simply a change in wind direction may explain the normal grading in the uppermost part of Unit III that is only evident in western outcrops. Compositionally, Unit III is the only stratigraphic unit with exclusively group A glass compositions. All other units are either a mixture of groups A and B or exclusively made out of higher evolved group B compositions. Correlation with the highest magma discharge rates found in Arce deposits may reflect compositional layering in the magma chamber and the tapping of a deeper situated magma of composition A, during evacuation of Unit III. Alternatively, the increase in lithic content and switch to only group A compositions may reflect a change in vent location and tapping of laterally distinct pods of these different magma compositions instead of compositional layering of the chamber. This problem cannot finally be solved but the compositional difference maybe induced by the injection of a more mafic magma batch shortly before the beginning of the eruption. This is evident through the increasing appearance of gray and banded trachytic/trachyandesitic pumices in Unit III and the seldom olivines occurring in the matrix and incorporated in the white pumices, often with a thin rim of the parental magma. Mixing of magma compositions is not observed anymore in the Upper Arce tephra maybe suggesting a homogenization of the magmas during the pause in the eruptions, or that the eruption only tapped the upper part of the magma chamber during LACT which become exhausted before UACT tapped then the now lower part. Further detailed petrological studies must confirm these hypotheses.

Unit IV is overall well-sorted and normal graded with an enrichment of hydrothermally altered and fresh lithics at the base and towards the top. The increasing amount of lithics possibly indicates an event of vent migration. The vent migration either might have happened without any break and can therefore be seen as a continuation of Unit III, or with a very short break in the eruption sequence shortly before the column stabilized again. The decreasing grain size indicates a slowly shrinking eruption column. Local differences can be explained by changing wind directions in the lower atmosphere (e.g., increase of grain sizes to the west) before final settling of the remaining dust that was dispersed in the air.

The appearance of Unit V varies regionally. In the West it is made of a single fine ash layer that probably represents continued deposition of fine ash from the atmosphere after emplacement of Unit IV. In this region the top of this layer is also strongly eroded. Proximal to the caldera in the North and East Unit V is emplaced as a poorly sorted, weakly laminated pinkish ash layer with lateral thickness variations and accretionary lapilli on top, and partly eroding into, a whitish ash layer similar to the west. Therefore, Unit V is interpreted here either as pyroclastic flow/surge deposits, or as a distal flow equivalent. They might indicate the last pulse of the eruption and subsequent collapse of the eruption column due to decreasing magma discharge rates or interaction between magma and ground water (e.g., accretionary lapilli) during the waning of the eruption. Alternatively, it just represents a ground-hugging ash cloud formed from slow settling of dust after the major fallout phase but the accretionary lapilli and lamination in the deposits argue more for the first interpretation. After Unit V in the whole region signs of erosion and development of an incipient soil is observed, which indicate a longer break in the eruption sequence after the emplacement of Unit V. This agrees well with the finding of the two distal Arce tephra layers in the lacustrine sediment sequence of Lake Petén Itzá (Fig. 6H, I), in the lowlands of Guatemala (Kutterolf et al., 2016).

Unit VI is the first unit after the pause in the eruption. In proximal outcrops the basal lithic-rich pumice lapilli layer mantles the eroded surface. This can be interpreted as an initial vent-cleaning event. The subsequent continuously growing, but slightly oscillating, eruption column emplaced massive, inversely graded, vaguely stratified pumice fallout.

The thick, widespread, massive, coarse (lapilli to block size) fallout Unit VII is emplaced in the entire region suggesting constant eruption conditions with a sustained high eruption column prevailing for considerable times. Larger amount of fresh lava lithics at the base suggest a vent-widening event in the beginning, setup of higher discharge rates, and consequently a higher eruption column. We speculate that the increasing amount and mixture of fresh and hydrothermally altered lithics in the normal graded uppermost part may be an evidence for vent migration and subsequently weakening of the eruption column rather than changes in the wind direction.

Grain sizes increase sharply from Units VII to Unit VIII in the north and east, which indicates development of a higher eruption column, although the appearance of Unit VIII varies regionally. Vertical grain size variations within beds suggest either small fluctuations in column height (e.g. partial collapses) or frequent changes in wind direction or local reworking during the long-lasting eruption phase. The appearance of a poorly sorted ash-rich deposit (lapilli tuff) exclusively to the west, with rounded, ash-coated pumice lapilli supports the interpretation of the emplacement of a distal pyroclastic flow deposit, generated by a partial eruption column collapse to the west, followed by a massive fallout.

Unit IX in north of the caldera clearly shows two different emplacement processes leading to alternating pumice/ash layers. Small changes in grain size of the first tripartite, irregular, partly (cross)stratified and poorly sorted ash bed suggest emplacement of several flow deposits, presumably from surges. These are followed by a moderately sorted ash- and lithic-rich fine to medium-lapilli fallout layer with some of its pumices impacted in the ash horizon below. This requires soft sediment, hence the ash deposit was wet. The sequence can be interpreted as a series of flow deposits from an oscillating, not well-developed and partly collapsing eruption column, possibly caused by a caving or migrating vent (lithic enrichment) and corresponding intrusion of ground water (e.g. accretionary lapilli). Finally, a more or less stable eruption column was reached that emplaced the fallout. The occurrence of rounded pumice clasts and the high ash content in the pumice layer may be the result of multiply interrupting small surge events. Subsequently, the eruption pulse weakens again causing normal gradation within the pumice layer. The second package of ash and pumice beds originated most probably by similar processes, although the lack of accretionary lapilli suggests a decreasing water influence.

The ignimbrite of Unit X consists of multiple flow units with decreasing thicknesses predominantly deposited toward the east and northeast where the Caldera rim is lowest; there is no evidence that the region to the West has been affected by meter-thick ignimbrite deposits like the east. This final eruptive stage was most probably associated with the caldera subsidence. The large erupted magma volume and absence of any fallout in the ignimbrite succession suggest emplacement by boiling over rather than collapsing eruption columns, generating morphology driven flow into the valley east of San Salvador volcano (Fig. 1).

In summary, based on the observations from proximal to medial sections, and composition the Arce sequence originated by two eruptions producing the Lower Arce Tephra (LACT; Units I to V), that is compositionally heterogeneous, and the Upper Arce Tephra (UACT; Units VI to X), that is compositionally homogeneous (Fig. 3, 4, 8). Another conclusion is that each of the sequences began with a pulsing eruption column, transitioned into a stable eruption column, but eruption column stability then decreased again and the eruption ended with the collapse of the eruption column.

### *4.2 Age inferences*

Stratigraphically the two Arce tephras as well as the Bella Vista eruption overlie the widely distributed deposits of the Los Chocoyos eruption (~84 ka; Atitlán Caldera, Guatemala). $^{40}$Ar/$^{39}$Ar age dating of sanidine revealed an age of 72 ± 3 for the Arce eruption and 77 ± 2 ka for the older Bella Vista eruption (Rose et al., 1999). Kutterolf et al. (2016) described the Upper and Lower Arce Tephra in the lacustrine sediments of Lake Petén Itza (Peten intervals 1B-16H-2, 72.2-72.5 and 75.4-78 cm; Peten 6B-19E-2, 106.4-106.8 and 111-112.4 cm). These two ash layers are separated by 3 to 4 cm of lacustrine sedimentation, which corresponds to approximately 120–460 years between the two eruptions assuming constant sedimentation rates. This short time period is of course not detectable by any radiometric dating techniques.

Zircon crystals from Lower and Upper Arce are mostly elongated (between 50 and 200 μm in length) and euhedral. Adherent glass was commonly observed in most of the crystals suggesting suspension in melt before eruption. $^{238}$U-$^{230}$Th model zircon rim ages of Lower Arce unit (n=57) range from ca. 71.1 $^{+15.6/-14.6}$ to 123 $^{+34/-30}$ ka (2σ), with the lower age boundary overlapping within analytical uncertainty to previously determined $^{40}$Ar-$^{39}$Ar sanidine eruption age (72 ± 4 ka, 2σ; Rose, 1999). Zircon ages for Upper Arce (64.3 to 110 ka) are within uncertainties indistinguishable from those of the lower unit (Fig. 10A). A common zircon population for both eruptions is further supported at high confidence by Kolmogorov-Smirnov statistical analysis (P = 0.88). Probability density diagrams show similar unimodal zircon age distributions with peaks at ca. ~80 ka (see Fig. 10A). Taking advantage of the U/Th variability among grains and the MSWD close to one for both samples, U-Th isochron free fit ages which are independent of initial U-Th whole-rock isotopic composition (Lowenstern et al., 2000) yielded an age of 83.1 ± 8.3 ka (2σ; MSWD = 1.3; n = 57) for Lower Arce and 80.1 ± 8.3 ka (2σ; MSWD = 0.94; n = 47) for Upper Arce (Fig. 10B). From the intercept of the isochron with the equiline, initial $(^{230}\mathrm{Th})/(^{232}\mathrm{Th})_0$ for Lower and Upper Arce of 0.728 +1.60/-1.35 and 1.125 +0.90/-1.17 (2σ), respectively, were obtained. For both samples the MSWD values associated with the linear regression are near unity, suggesting that zircon rim crystallization occurred at relatively short timescales commensurate to those of their uncertainty. For both samples no xenocrystic zircon (with ages in secular equilibrium) were detected. Zircon U abundances are similar for both samples (~60-1700 ppm; average= 368 ppm). The coeval wide range of U abundances suggests concurrent regions in the magma chamber with differing degrees of crystallinity tapped in the awake of the eruption.

Zircon rim ages usually represent the latest crystallization events before eruption, therefore, their appearance at the surface is considered as representative for a maximum depositional age that can predate eruption by a few to several thousands of years. In the case of the Arce tephra zircons, although the mean of all zircon data may indicate slightly older ages for LACT, isochron ages for the two individual eruptions indicate no resolvable age difference but rather overlapping maximum depositional ages that are within uncertainties to the previously postulated eruption age of 72 ka ($^{40}Ar/^{39}Ar$; Rose et al 1999). The overlapping unimodal zircon age spectra from both eruptions peak at ca. 80 ka (Fig. 10B) suggesting relatively rapid and enhanced differentiation (within ca. 8 kyr uncertainty from isochron ages) from a common magmatic reservoir just a few thousands of years prior to eruption. This is further supported by higher U contents in zircon prior to eruption.

In summary, field observations (initial incipient soil, unconformity), and lacustrine and Caribbean sediment cores (two discrete ash layers separated by background sediment) in addition to the unresolvable zircon age differences give strong evidence that Arce had two eruptions in close succession and separated by a pause in eruption of only several hundred years. It is noteworthy that the age of the two Arce eruptions and the Bella Vista eruption overlap within the errors. The temporal proximity might explain the geochemical affinity between the Lower Arce Unit I and the Bella Vista Tephra. The Bella Vista tephra is a very locally confined deposit that consists of a high amount of glassy lava dome fragments featuring the chemical composition of the Bella Vista Tephra and Lower Arce Tephra Unit I. Therefore, the Bella Vista eruption can probably be interpreted as an initial conduit clearing precursor stage of the Arce eruption, after a dome growing phase or the system was, at that stage, an interconnected set of dikes and sills that remained isolated during the first event (cf. magma system model of Cashman and Giordano 2014). Further petrological studies must confirm this hypothesis.

### ***4.3 Tephra distribution and eruption dynamics***

Previously determined distribution area, volume, erupted magma mass, mass discharge rate and eruption column height from bulk-Arce Tephra isopach and isopleth maps ($1.8 \times 10^5$ km$^2$, 17.9 km$^3$, 2.2 $\times 10^{13}$ kg, $1 \times 10^9$ kg/s, 35 to 40 km; Kutterolf et al., 2008b, 2016) represent minimum values for the total Arce eruption. Here, we apply the same approach to stratigraphic units of the Arce Tephra in order to investigate temporal changes in eruption conditions and finally distinguish eruption parameters for the Lower and Upper Arce Tephra eruptions. Since not all units can be traced throughout the medial facies, and some show strong lateral changes due to their mode of flow emplacement, we determine the areal distribution characteristics for tephra packages differently. For all Units I through Unit IX we used thickness values to construct isopach maps (Fig. 9 C-F). For Units II – IV and Units VI to VIII we used maximum grain sizes (MP, ML) measured in the field to construct isopleth maps (Fig. 9G,H). Proximal tephra volumes of the individual units (VP) are minimum estimates of proximal and medium outcrops since we cannot trace individual units into the distal facies (Fig. 9B, Table 1). For comparison, volumes for integrated proximal to distal outcrops (VT) have been estimated where also a proximal/medial portion (VTp) and distal portion (VTd) can be distinguished (Fig. 11).

VP´s of units I to IX together account for 21% of VT´s for UACT and LACT together (94% of total VTp´s for both Arce eruptions; Table 1, Figure 11). VTd´s of the two eruptions account for 80% (LACT) and 69% (UACT) of the respective VT´s, excluding the ignimbrite volume that represents roughly a third of VT of the UACT (Table 1).

Major medial to proximal volumes include Plinian fall Units II (0.8 km$^3$), III (3 km$^3$), and IV (0.8 km$^3$) from the Lower Arce eruption and Units VI (1 km$^3$), VII (5 km$^3$), and VIII (1.9 km$^3$) from the Upper Arce eruption. Initial Unit I (0.1 km$^3$) as well as Units V and IX of the eruptions contribute little to the respective total erupted volumes.

The comparisons of isopleth ranges with model predictions (Figs. 12, 13) yield estimates of eruption column heights and mass discharge rates that are summarized in Figure 14a. While the absolute values of these parameters remain quite uncertain due to incomplete constraints of the isopleth maps and simplifying model assumptions, the relative changes between eruption units are better constrained. The accuracy of the results depends mainly on the shape and area of the isopleths, which are controlled by wind strength and direction. Since isopachs are also controlled by those two parameters, but are constrained by much more data, similar shapes of the isolines in one unit are also an indirect proof for the validity of the isopleth data.

Discharge rates, erupted volume, and column height increased during Plinian eruption phases from Unit I to III of LACT (Fig. 14B), reaching peak values during emplacement of Unit III before they decreased again from Unit IV to probably Unit V. As a result, estimated minimum duration of the eruption phases decreased from the order of 4 hours for Unit II to less than 1 hour for Unit III, although the latter alone accounts for at least 60% of the total erupted tephra volume (Vp) determined for the individual LACT units together. The Upper Arce eruption developed differently (Fig. 14B). The highest eruption column, and the maximum discharge rate of Unit VI does not coincide with the highest erupted volume and an overall continuous column height decrease from Unit V to Unit VIII is observed. Therefore, the eruption duration inferred from erupted volume and discharge rate, increases continuously from 0.5 hours for Unit VI to more than 7 hours for Unit VIII.

In summary, the Lower (25.6 km$^3$) and Upper (40.5 km$^3$) Arce eruptions account for 66.1 km$^3$ of erupted tephra volume (33 km$^3$ DRE) and the individual eruptions lasted on average at least 30 and 72 hours. In addition, the ignimbrite produced during Unit X accounts for 10 km$^3$ of erupted PDC volume. The total erupted volume of both eruptions together is one third larger than the volumes determined so far for the Arce event.

### *4.4. Hazard impact*

Volcanic hazards constitute a pervasive threat in northwestern El Salvador. Next to the more frequent, but generally small eruptions from Santa Ana, larger explosive eruptions from the Coatepeque Caldera are conceivable in future. Although the last activity of the Coatepeque

Caldera has taken place ~51,000 years ago (Conacaste eruption), future eruptions cannot be excluded since large volcanic systems have larger recurrence times than the usual, recently active arc volcanoes (e.g., Mason et al., 2004; Brown et al., 2014).

We cannot predict or forecast if and when a future eruption at the Coatepeque Caldera will occur, but we can evaluate what eruptions of a similar size would cause in this vulnerable region. Evaluating the isopach maps (Fig. 9) the most vulnerable zone is of course in the direct vicinity (~5 km) of the caldera. But vulnerability is still high in the area of Santa Ana, one of the biggest cities in El Salvador and only ten kilometers away from the caldera. During the Arce eruptions, both, pyroclastic falls (50 to 200 cm) and flows (0.5 to 3 m) have been deposited in this area (Fig. 9).

Distal fallouts are another often-neglected threat for the population. With respect to the average roof construction in Central America, fallout thicknesses of ~10 cm (distribution area of 500 to 10.000 km$^2$ per Unit; Fig. 11), or even less for compacted wet tephra, are probably sufficient to cause roof collapse in response to rapid accumulation in the wider area around the caldera (e.g., Freundt et al., 2006b). Assuming the same tropospheric and stratospheric wind conditions as today (see discussion in Kutterolf et al., 2007) especially the densely populated towns of St Anna, Chalchupa and Sonsonate located northwest and southwest of the Caldera are vulnerable, depending on the season of an eruption. Beside these directly eruption related hazards, the atmospheric (e.g. Brenna et al. 2019) and environmental impact, as for example distal ash induced crop failures (e.g. Kakani et al., 2003; Teramura, 1983), pollution of water (e.g. Häder et al. 1995), and the long-lasting effect of remobilized fine glass shards causing silicosis (e.g. Horwell and Baxter 2005), may affect the society for years after such an eruption.

## 5 Summary

The 72 ka old Arce tephra sequence from Coatepeque Caldera is the product of a temporally close-spaced double eruption within a couple of hundreds of years subdivided stratigraphically and compositionally into the Lower and Upper Arce Tephra. Compositional variations within and between the eruptions as well as partly admixed trachytic pumice clasts in the Lower Arce Tephra suggest a zoned magma chamber or two parallel existing reservoirs where the Arce magma reservoir(s) may probably be influenced by a more mafic magma batch shortly before the eruption and interact between the layering or between each reservoir. Magmas are variably tapped during eruptions due to changing magma discharge rates and/or vent migration. Both eruptions started with a series of fallout units featuring stable eruption columns in the main eruptive phase as well as fluctuating and partially collapsing eruption columns in the beginning and to the end. Lower Arce eruption ceased with an ash layer, maybe surge related, that was partly eroded and shows signs of overlying indurated soil development. In contrast the surge deposits at the end of Upper Arce Tephra point to several, repeating eruption collapses (deposits) that most probably ended in a final, catastrophic, caldera collapse and emplacement of the thick ignimbrite. Mapping of the individual eruptive phases including the occurrences of distal marine and lacustrine ash layer in the Pacific, the Guatemalan lowlands and the Caribbean Sea, resulted in eruptive volumes that sum up to a total of 25.6 km$^3$ and 40.5 km$^3$ tephra volume, including the ignimbrite volume of 10km$^3$, and eruption column heights between 20 - 33 km for the Lower and Upper Arce eruption, respectively. The distribution maps show what potential hazards from eruptions of a similar size from Coatepeque Caldera may anticipated in this vulnerable region and even in the distal region around San Salvador.

Finally, the new findings that Arce eruption is a temporally close-spaced double eruption have a brought impact for regional stratigraphy since the very prominent Arce deposits are widely accepted marker horizons for geology and archeology.

## Acknowledgement

We gratefully acknowledge the support by the Observatorio Ambinetal of the Ministerio de Medio Ambiente y Recursos Naturales (MARN) in San Salvador, particularly by the director

Celina Kattan de Soto for logistic assistance, as well as all the colleagues who accompanied us during field work. SK and JS acknowledge the German Research foundation (KU2685/2-2 and 7-1) for supporting this work. We also want to thank you Mario Thöner, and Fu-Lung Lin who helped with the analyses at the electron microprobe at GEOMAR and the LA-ICP-MS in Taiwan respectively. We also appreciate the comments and suggestions from Dr. Heather Wright and one anonymous reviewers, which helped to improve the manuscript.

## References

Agostini, S., Corti, G., Doglioni, C., Innocenti, F., Tonarini, S., Manetti, P., Di Vincenzo, G. and Montanari, D., 2006. Tectonic and magmatic evolution of the active volcanic front in El Salvador: insight into the Berlín and Ahuachapán geothermal areas. Geothermics, 35(4): 368-408.

Blake S, Ivey GN (1986) Magma-mixing and the dynamics of withdrawal from stratified reservoirs. J Volcanol Geotherm Res 27: 153-178

Brenna, H., Kutterolf, S., Krüger K., (2019) Global ozone depletion and increase of UV radiation caused by pre-industrial tropical volcanic eruptions. Scientific Reports, 9:9435, DOI: 10.1038/s41598-019-45630-0

Brown, S.K., Crosweller, H.S., Sparks, R.S.J., Cottrell, E., Deligne, N.I., Guerrero, N.O., Hobbs, L., Kiyosugi, K., Loughlin, S.C., Siebert, L. and Takarada, S., 2014. Characterisation of the Quaternary eruption record: analysis of the Large Magnitude Explosive Volcanic Eruptions (LaMEVE) database. Journal of Applied Volcanology, 3(1): 5.

Cashman, K.V. and Giordano, G., 2014. Calderas and magma reservoirs. J Volcanol Geotherm Res, 288: 28-45.

Carey, S. and Sparks, R.S.J., 1986. Quantitative models of fallout and dispersal of tephra from volcanic eruption columns. Bull Volcanol 48:109–125

CEL, 1992. Desarrollo de los Recursos Geotermicos del Area Centro-Occidental de El Salvador. Prefactibilidad Geotermica del Area de Coatepeque. Reconocimiento Geotermico. contrado 344, Commision Ejecutiva Hidroelectrica del Rio Lempa, San Salvador.

DeMets, C., 2001. A new estimate for present-day Cocos-Caribbean plate motion: Implications for slip along the Central American volcanic arc. Geophys. Res. Lett., 28: 4043-4046.

Fierstein, J., Houghton, B.F., Wilson, C.J.N. and Hildreth, W., 1997. Complexities of plinian fall deposition at vent: An example from the 1912 Novarupta eruption (Alaska). J Volcanol Geotherm Res, 76: 215-227.

Fierstein, J. and Nathenson, M., 1992. Another look at the calculation of fallout tephra volumes. Bull. Volcanol., 54: 156-167.

Freundt, A., Kutterolf, S., Schmincke, H.U., Hansteen, T.H., Wehrmann, H., Perez, W., Strauch, W. and Navarro, M., 2006. Volcanic hazards in Nicaragua: Past, present, and future. In: W.I. Rose, G.J.S. Bluth, M.J. Carr, J. Ewert, L.C. Patino and J.W. Vallance (Editors), Volcanic hazards in Central America. Geol. Soc. Am. Spec. Publ., pp. 141-165.

Garbe-Schönberg, C.-D., 1993. Simultaneous determination of thirty-seven trace elements in twenty-eight international rockstandards by ICP-MS. Geostandards Newsletter, 17(1): 81-97.

Günther, D., Jackson, S.E. and Longerich, H.P., 1999. Laser ablation and arc/spark solid sample introduction into inductively coupled plasma mass spectrometers. Spectrochimica Acta Part B: Atomic Spectroscopy, 54(3): 381-409.

Häder, D.-P., Worrest, R. C., Kumar, H. D. & Smith, R. C. Effects of Increased Solar Ultraviolet Radiation on Aquatic Ecosystems. Ambio 24, 174–180 (1995).

Horwell, C.J. and Baxter, P.J. (2006) The respiratory health hazards of volcanic ash: a review for volcanic risk mitigation. Bull Volcanol, 69:1-24, DOI 10.1007/s00445-006-0052-y

Houghton BF, Wilson CJN, Pyle DM (2000) Pyroclastic fall deposits. In: Sigurdsson et al. (eds) Encyclopedia of volcanoes. Academic Press, pp 555–570

Kakani, V. G., Reddy, K. R., Zhao, D. & Sailaja, K. Field crop responses to ultraviolet-B radiation: A review. Agric. For. Meteorol. 120, 191–218 (2003).

Kitamura, S., 2017. Temporal chemical variation of the Arce tephra from Coatepeque Caldera, El Salvador, Central America. Bulletin of Faculty of Social Work, Hirosaki Gakuin University, Vol 17, 21-30.

Kutterolf, S., Freundt, A., Peréz, W., Wehrmann, H. and Schmincke, H.-U., 2007. Late Pleistocene to Holocene temporal succession and magnitudes of highly-explosive volcanic eruptions in west-central Nicaragua. J. Volc. Geo. Res., 163: 55-82.

Kutterolf, S., Freundt, A., Peréz, W., Mörz, T., Schacht, U., Wehrmann, H. and Schmincke, H.-U., 2008a. The Pacific offshore record of Plinian arc volcanism in Central America, part 1: Along-arc correlations. Geochem. Geophys. Geosyst., 9(2): doi:10.1029/2007GC001631.

Kutterolf, S., Freundt, A. and Peréz, W., 2008b. The Pacific offshore record of Plinian arc volcanism in Central America, part 2: Tephra volumes and erupted masses. Geochem. Geophys. Geosys., 9(2): doi:10.1029/2007GC001791.

Kutterolf, S., Freundt, A. and Burkert, C., 2011. Eruptive history and magmatic evolution of the 1.9 ka Plinian dacitic Chiltepe Tephra from Apoyeque volcano in west-central Nicaragua. Bull Volcanol, 73: 811-831.

Kutterolf, S., Schindlbeck, J.C., Anselmetti, F.S., Ariztegui, D., Brenner, M., Curtis, J., Schmid, D., Hodell, D.A., Mueller, A., Pérez, L., Pérez, W., Schwalb, A., Frische, M. and Wang, K.L., 2016. A 400-ka tephrochronological framework for Central America from Lake Petén Itzá (Guatemala) sediments. Quaternary Science Reviews, 150: 200-220.

Le Maitre, R.W., Streckeisen, A., Zanettin, B., Le Bas, M., Bonin, B. and Bateman, P., 2002. Igneous Rocks: A Classification and Glossary of Terms: Recommendations of the International Union of Geological Sciences Subcommission on the Systematics of Igneous Rocks. Cambridge University Press, Cambridge.

Lowenstern, J., Persing, H., Wooden, J., Lanphere, M., Donnelly-Nolan, J., Grove, T., 2000. U–Th dating of single zircons from young granitoid xenoliths: new tools for understanding volcanic processes. Earth and Planetary Science Letters 183, 291-302.

Ludwig, K., 2003. User's manual for Isoplot 3.00: a geochronological toolkit for Microsoft Excel. Berkeley Geochronology Center Special Publication.

Martínez-Díaz, J.J., Álvarez-Gómez, J.A., Benito, B.n. and Hernández, D., 2004. Triggering of destructive earthquakes in El Salvador. Geology, 32(1): 65-68.

Mason, B.G., Pyle, D.M. and Oppenheimer, C., 2004. The size and frequency of the largest explosive eruptions on Earth. Bull Volcanol, 66: 735-748.

Paladio-Melosantos, L.O., Solidum, R.U., Scott, W.E., Quiambao, R.B., Umbal, J.V., Rofdolfo, K.S., Tubianosa, B.S., Reyes, P.J.D., Alonso, R.A., Ruelo, H.B., 1996. Tephra falls of the 1991 eruptions of Mount Pinatubo. In: Newhall CG, Punongbayan RS (eds) Fire and mud: eruptions and lahars of Mount Pinatubo, Philippines. USGS, Hong Kong, pp 325–332

Pyle, D.M., 1989. The thickness, volume and grain size of tephra fall deposits. Bull. Volcanol., 51: 1-15.

Rabek, K., Ledbetter, M.T. and Williams, D.F., 1985. Tephrochronology of the Western Gulf of Mexico. Quaternary Research, 23: 403-416.

Reid, M.R., Coath, C.D., Mark Harrison, T., McKeegan, K.D., 1997. Prolonged residence times for the youngest rhyolites associated with Long Valley Caldera:230Th—238U ion microprobe dating of young zircons. Earth and Planetary Science Letters 150, 27-39.

Rose, W.I., Conway, F.M., Pullinger, C.R., Deino, A. and McIntosh, K., 1999. An improved age framework for late Quaternary silicic eruptions in nothern Central America. Bull. Volcanol., 61: 106-120.

Rudnick, R.L., Fountain, D.M., 1995. Nature and composition of the continental crust: a lower crustal perspective. Reviews of Geophysics 33, 267-309.

Ryan, W. B. F., Carbotte, S. M., Coplan, J. O., O’Hara, S., Melkonian, A., Arko, R., et al. (2009). Global multi-resolution topography synthesis. Geochemistry, Geophysics, Geosystems, 10, Q03014. https://doi.org/10.1029/2008gc002332

Schindlbeck, J.C., Kutterolf, S., Freundt, A., Eisele, S., Wang, K.L. and Frische, M., 2018. Miocene to Holocene Marine Tephrostratigraphy Offshore Northern Central America and Southern Mexico: Pulsed Activity of Known Volcanic Complexes. Geochemistry, Geophysics, Geosystems, 19(11): 4143-4173.

Siebert, L., Simkin, T. and Kimberly, P., 2010. Volcanoes of the World: Third Edition. University of California Press.

Schmitt, A.K., 2011. Uranium series accessory crystal dating of magmatic processes. Annual Review of Earth and Planetary Sciences 39, 321-349.

Schmitt, A.K., Vazquez, J.A., 2017. Secondary ionization mass spectrometry analysis in petrochronology. Reviews in Mineralogy and Geochemistry 83, 199-230.

Schmitz, M.D., Bowring, S.A., Ireland, T.R., 2003. Evaluation of Duluth Complex anorthositic series (AS3) zircon as a U-Pb geochronological standard: new high-precision isotope dilution thermal ionization mass spectrometry results. Geochimica et Cosmochimica Acta 67, 3665-3672.

Stoppa, L., Kutterolf, S., Rausch, J., Grobety, B., Pettke, T., Wang, K.-L. and Hemming, S., 2018. The Malpaisillo Formation: A sequence of explosive eruptions in the mid to late Pleistocene (Nicaragua, Central America). Journal of Volcanology and Geothermal Research, 359: 47-67.

Teramura, A. H. Effects of ultraviolet-B radiation on the growth and yield of crop plants. Physiol. Plant. 58, 415–427 (1983).

Wilson. L., and Walker, G.P.L., 1987. Explosive volcanic eruptions-VI. Ejecta dispersal in plinian eruptions: the control of eruption conditions and atmospheric properties. Geophys Journal of Royal Astronomic Society, 89:657–679.

Woods, A.W., 1988. The fluid dynamics and thermodynamics of eruption columns. Bull Volcanol 50:169–193

Table 1: Eruption parameter for the Arce Tephra divided into individual stratigraphic units (Vp), their cumulative eruptive parameter summarized also in Lower and Upper Arce numbers and comparison to eruptive parameter (e.g. volumes; VT) determined by using integrated isolines for Upper and Lower Arce and their consideration in distal and proximal areas.

Supplementary Figure 1: Detailed section description of selected Arce profiles including all profiles and a legend (in the order from a to m: Arce 6, E66, Arce 21, E31, Arce 4, 8, 23, 43, 1, 10, 31, 13, 14) shown in Figure 5.

Supplement table 1: outcrop locations and sample list

Supplement table 2: thickness and MP, ML of each unit and outcrop

Supplement table 3: Bulk rock compositions of selected samples from XRF and solution ICP-MS

Supplement table 4: glass compositions of selected samples measured by electron microprobe and LA-ICPMS

Supplement table 5: LA-ICPMS U-Th results for Lower and Upper Arce composite pumice samples (whole-rock).

## Figure Captions

Figure 1: A) Overview map of El Salvador and neighboring countries with the major volcanic regions in southern Guatemala and El Salvador as well as the continental slope and Pacific Ocean to the south. B) Close up of the Coatepeque region with black circles and numbers representing the investigated outcrops. Red dot represents the Coatepeque volcanic complex, gray dots the modern volcanic front (Siebert et al. 2010), roads are marked in yellow. Map created using GeoMapApp (http://www.geomapapp.org; GMRT-Global Multi-Resolution Topography) (Ryan et al., 2009).

Figure 2: Composite profile for the Arce tephra sequence with corresponding stratigraphic units their brief description. The layer thicknesses are not representative for all outcrops but reflect relative thickness relations in the field at medial distances. Dot-dashed line represents the break

between Lower and Upper Arce Tephra, solid lines the boundaries between the stratigraphic units.

Figure 3: Total alkali versus silica plot with volcanic rock classes after Le Maitre et al. (2002) to indicate matrix-glass compositional ranges of Arce tephra units (normalized to anhydrous compositions, averages per sample). The analyzed glass shards cluster into two major compositional groups A and B within the rhyolite field; exception is the average of the gray pumices of Units II and III that fall in the trachytic field. The colors, given in the legend, represent the Lower (blue) and Upper (purple) Arce tephras and the symbols reflect the different stratigraphic units. Additionally, the glass compositions of the other Coatepeque eruptions are plotted (gray stars) as well as the bulk rock data for Arce tephra.

Figure 4: Discrimination diagrams indicating the differences between the two compositional groups as well as their stratigraphic variability using FeOt and $Na_2O$ versus $SiO_2$ (A, B), $K_2O$ versus CaO (C), Ba/La versus Rb/Hf (D), and Ba/Zr versus Zr/Nb (E) plots. Insets extend the range of the element concentrations to the tracytic and trachyandesitic samples (arrows indicate trachyandesite (TA) and trachyte (T)) and show their genetic relationship to the Arce glass and whole rock data (grey fields). F) and G) indicate stratigraphic variations in composition at the example of CaO and Ba/La. In all diagrams a clear distinction between group A and B can be observed. UACT is exclusively made out of group B compositions with the exception of the ignimbrite that also shows group A compositions. Major element data are averaged per sample and standard deviation is within symbol size. Trace element data are single glass shard analyses for all samples, only marine samples from Petén Itza (Kutterolf et al., 2016) are averages and the gray bars show the standard deviation for these samples.

Figure 5: Correlations and thickness variations between the single stratigraphic units of the Arce deposits on NNE/SSW and W/E lines. For explanation of the filling pattern see Figure 2.

Figure 6: Overview pictures showing the Arce tephra sequence. A) Medial to distal outcrop showing entire LACT, and the lower part (Units VI and VII) of UACT Northeast of the caldera (A01). The white ash layer in the middle marks the boundary between LACT and UACT. B) Proximal tephra sequence with falls and thick ignimbrite southeast of the caldera (A23). C) Proximal upper part of LACT (Units III to V) and UACT east of the caldera (A42). D) Lowermost proximal Lower Arce units east of the caldera (A03). E) Distal Ignimbrite deposit with three flow units northeast of the caldera (A14). F) Lapilli pipes in flow units at distal outcrop A14. G) Proximal unit I and lithic rich base of Unit II at outcrop A03. H) and I) sediment cores from Petén Itzá ICDP drilling. In both core pictures a thicker (1 to 3 cm) lower ash layer can be observed overlain by lacustrine sediments and another thin (1 to 5 mm) ash layer representing Lower and Upper Arce Tephra as inferred by proofed by chemical finger printing in Kutterolf et al. (2016).

Figure 7: Detailed pictures for Lower Arce tephra. A) Entire LACT from Unit I to V and lower most Unit VI of UACT at distal outcrop A08. B) Transition between LACT and UACT with units III (upper part), IV, V, VI, and VII in Santa Anna (A21). C) Units IV, Va, Vb, VI at medial outcrop 21 to the north of the caldera showing Lithic enrichment within the upper part of Unit IV, the normal gradation and the two ash layers of unit V. D) Close up of ash layers and erosional surface of Unit V (A08). E) Close up of Unit V at A21 showing a two partite ash layer with rounded pumice clasts included in the pink ash. F) Transition from Units VII to VIII in the west (A08), showing normal grading on top of unit VII and fine ash layer with variable thickness at the base of Unit VIII. G) Units VII to X in medial outcrop A21 showing the more massive and slightly coarser Unit VIII after the normal graded top of Unit VII, the two tripartite tephra sequences of Unit IX, and the lower part of the ignimbrite from Unit X. H) same sequence like in G) but in proximal outcrop E31. I) Flow units, pumice enriched lenses and unconformities within Unit X at outcrop A13

Figure 8: Schematic eruptive sequence for the Arce eruptions indicating dominant emplacement processes for each respective stratigraphic unit and partly subunits. The color code refers to stratigraphic units as presented in figures 10 to 14. Note: eruption column heights are just estimated and shown relative between the individual tephra units to reflect changes in thicknesses and grains sizes between them.

Figure 9: A Proximal to medial location map of the Coatepeque area with locations of outcrops used here (see supplementary table 1). Pinkish area outlines the extend and approximate thickness of the Unit X ignimbrite. B Ln (isopach thickness) versus square-root (isopach area) diagram for the units mapped in C to F). Linear regressions as indicated were used to calculate tephra volumes (listed in inset box) after Fierstein and Nathenson (1992). Data from Pinatubo 1991 and Mt. St. Helens 1980 (MSH) from Houghton et al. (2000) and Paladio- Melosantos et al. (1996) are shown for comparison. C to F Isopach maps, and G to H isopleth maps for ArceTephra units. Solid lines are well constrained, dashed lines are estimated. Filled circles indicate locations of reliable measurements used for the isolines.

Figure 10: A) Rank-order and relative probability plots for U-Th crystallization ages for zircon rims showing unimodal distribution of individual crystallization ages for zircons from Upper Arce Tephra (n=47; red symbols and lines) and Lower Arce Tephra (n=57; green symbols and lines). Eruption $^{40}$Ar/$^{39}$Ar sanidine age from Rose (1999). B) Isochron diagram plotting ($^{230}$Th)/($^{232}$Th) versus ($^{238}$U)/($^{232}$Th) for Lower and Upper Arce pumice zircons. Regression lines are calculated considering X and Y errors ($2\sigma$).

Figure 11: Distal isopach areas for Lower (A) and Upper (B) Arce tephra. Thicknesses for marine and lacustrine tephras are from Kutterolf et al. (2008a,b, 2016) and Schindlbeck et al. (2016, 2018). C. Ln (isopach thickness) versus square-root (isopach area) diagram for Lower and Upper Arce Tephra. Linear regressions as indicated were used to calculate tephra volumes (listed in inset box) after Fierstein and Nathenson (1992). Linear Regressions and respective

calculated volumes for a single, not subdivided, Arce tephra taken from Kutterolf et al,. (2016) for comparison where ash distribution to the Northwest was interpreted to be related to co-ignimbrite ash.

Figure 12: Diagrams of crosswind range versus downwind range for ML and MP isopleth data of the different stratigraphic Arce tephra units compared to model results of Carey and Sparks (1986). Clasts were selected to be close to, but are not identical to, the diameter×density products shown. The range of pumice and lithic sizes are given in diagrams and we used densities given in Supplementary Table 1. Horizontal grid lines indicate eruption column heights (in km) and diagonal grid lines show wind velocities (in m/s). Half-split symbols indicate the same values for two different units distinguished by the representative unit color. Lower and Upper Arce symbols represent values retrieved from summarized isopleths for each eruption.

Figure 13: MP and ML clast size×density versus isopleth cross-wind range of the stratigraphic Arce tephra units compared to model results of Wilson and Walker (1987). Note that model results below the dashed line are less reliable since Wilson and Walker used a top-hat velocity profile that did not capture lateral velocities in the higher part of the eruption column.

Figure 14: Diagram of logarithm of mass eruption rate versus eruption column height in which the ellipses show the range of data for each Arce unit. Black curves show modelled variation for temperatures of 800 K and 1200 K after Woods (1988). Results for the Arce units define a separate curve, similar to the Nicaraguan tephras in Kutterolf et al. (2007). Stars indicate data of Pinatubo 1991 and Mt. St. Helens 1980 (MSH) eruptions from Houghton et al. (2000) and Paladio-Melosantos et al. (1996) for comparison. b Comparison of eruption parameters and their changes upward through the Arce successions. Bold dashed line marks the boundary between Lower and Upper Arce Units. Eruption durations are minimum estimates determined by dividing erupted masses by respective eruption rates. Stratigraphic compositional variations

are given by black boxes representing compositional group A and white boxes representing compositional group B.

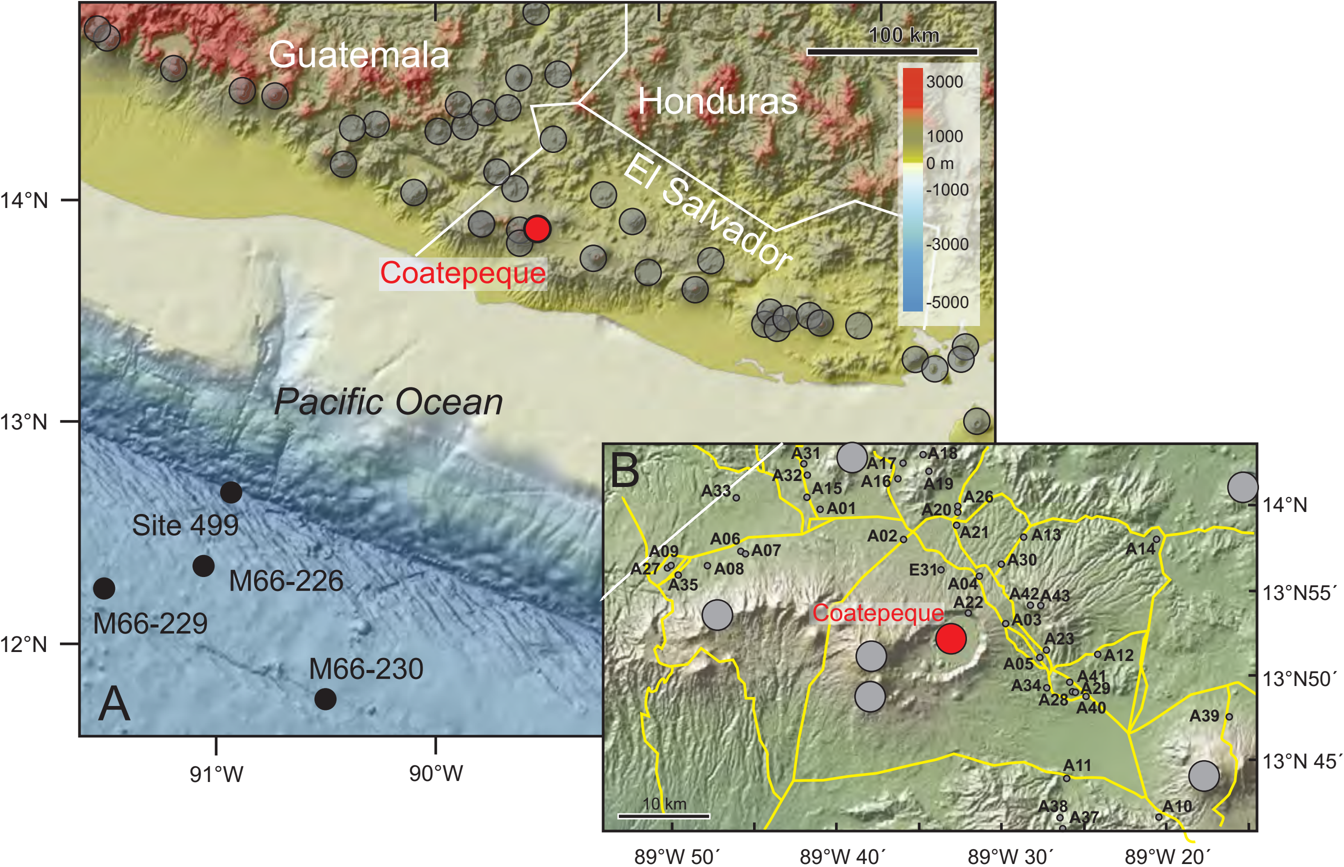
A
Guatemala
Honduras
El Salvador
Coatepeque
Pacific Ocean
100 km
3000
1000
0 m
-1000
-3000
-5000
Site 499
M66-226
M66-229
M66-230
14°N
13°N
12°N
91°W
90°W
B
A31
A17
A18
A32
A16
A19
A33
A15
A01
A26
A20
A21
A02
A13
A06
A09
A07
A14
A27
A08
A30
E31
A35
A04
A42
A43
A22
Coatepeque
A03
A23
A12
A05
A41
A34
A29
A28
A40
A39
A11
A38
A37
A10
10 km
14°N
13°N55´
13°N50´
13°N 45´
89°W 50´
89°W 40´
89°W 30´
89°W 20´

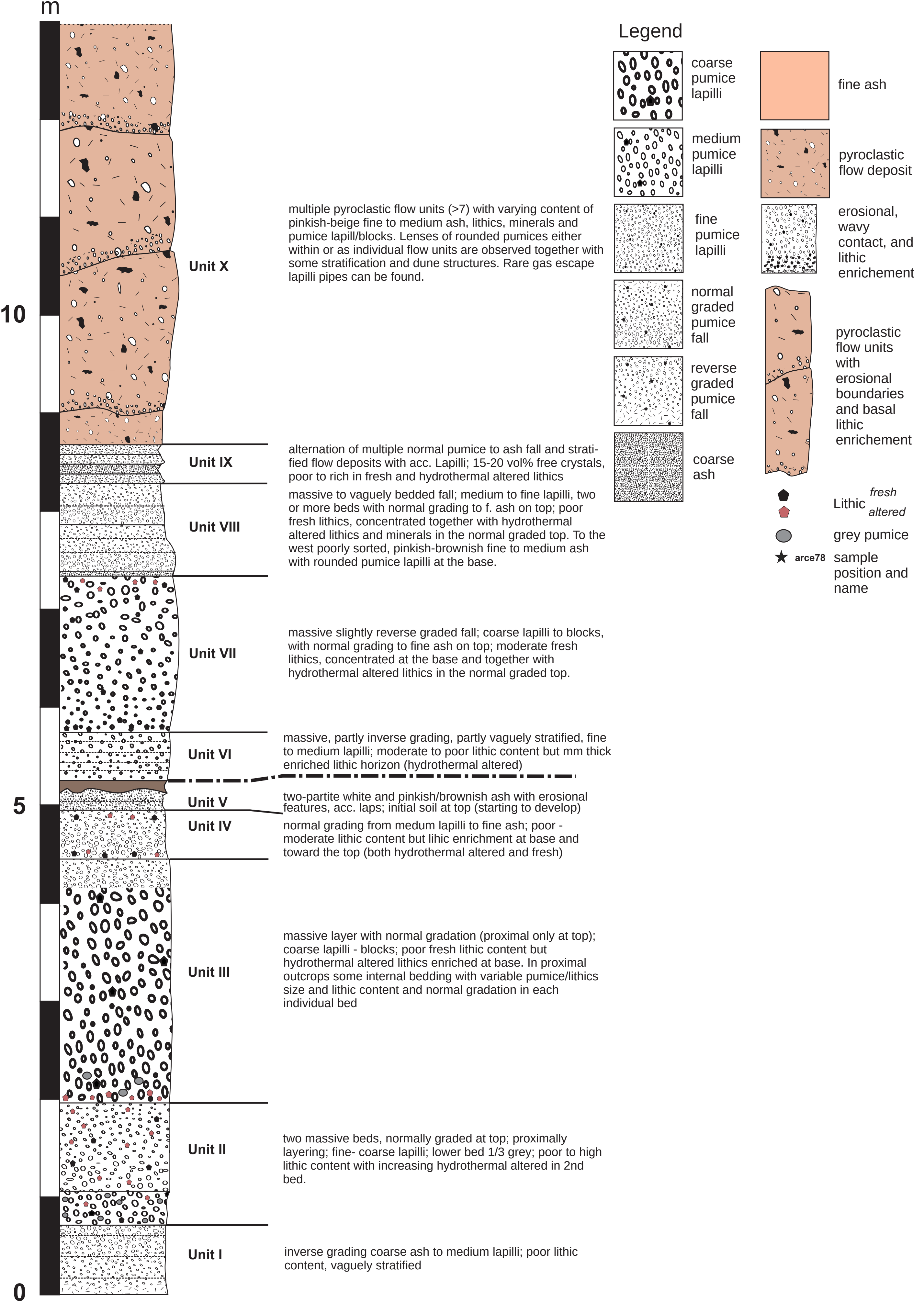

Unit X: multiple pyroclastic flow units (>7) with varying content of pinkish-beige fine to medium ash, lithics, minerals and pumice lapill/blocks. Lenses of rounded pumices either within or as individual flow units are observed together with some stratification and dune structures. Rare gas escape lapilli pipes can be found.

Unit IX: alternation of multiple normal pumice to ash fall and stratified flow deposits with acc. Lapilli; 15-20 vol% free crystals, poor to rich in fresh and hydrothermal altered lithics

Unit VIII: massive to vaguely bedded fall; medium to fine lapilli, two or more beds with normal grading to f. ash on top; poor fresh lithics, concentrated together with hydrothermal altered lithics and minerals in the normal graded top. To the west poorly sorted, pinkish-brownish fine to medium ash with rounded pumice lapilli at the base.

Unit VII: massive slightly reverse graded fall; coarse lapilli to blocks, with normal grading to fine ash on top; moderate fresh lithics, concentrated at the base and together with hydrothermal altered lithics in the normal graded top.

Unit VI: massive, partly inverse grading, partly vaguely stratified, fine to medium lapilli; moderate to poor lithic content but mm thick enriched lithic horizon (hydrothermal altered)

Unit V: two-partite white and pinkish/brownish ash with erosional features, acc. laps; initial soil at top (starting to develop)

Unit IV: normal grading from medum lapilli to fine ash; poor - moderate lithic content but lihic enrichment at base and toward the top (both hydrothermal altered and fresh)

Unit III: massive layer with normal gradation (proximal only at top); coarse lapilli - blocks; poor fresh lithic content but hydrothermal altered lithics enriched at base. In proximal outcrops some internal bedding with variable pumice/lithics size and lithic content and normal gradation in each individual bed

Unit II: two massive beds, normally graded at top; proximally layering; fine- coarse lapilli; lower bed 1/3 grey; poor to high lithic content with increasing hydrothermal altered in 2nd bed.

Unit I: inverse grading coarse ash to medium lapilli; poor lithic content, vaguely stratified

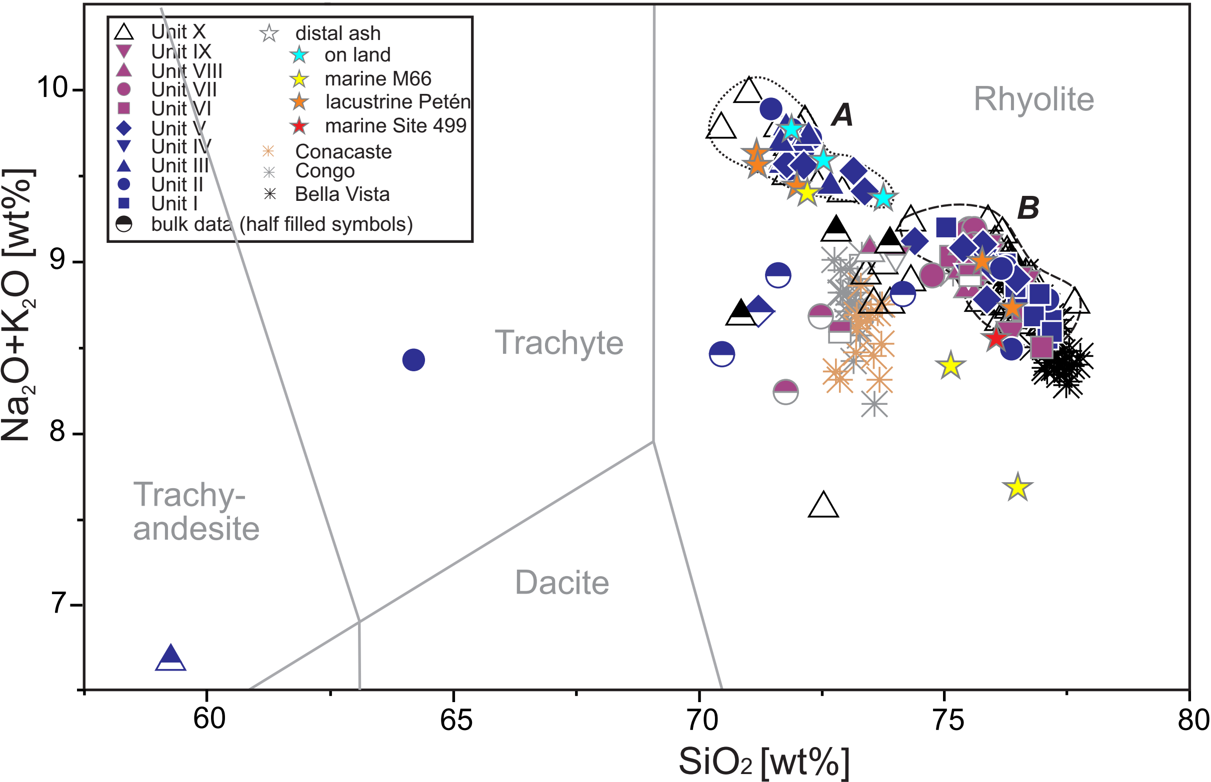
Unit X
Unit IX
Unit VIII
Unit VII
Unit VI
Unit V
Unit IV
Unit III
Unit II
Unit I
bulk data (half filled symbols)
distal ash
on land
marine M66
lacustrine Petén
marine Site 499
Conacaste
Congo
Bella Vista
A
B
Rhyolite
Trachyte
Trachy-andesite
Dacite
10
9
8
7
60
65
70
75
80
$Na_2O+K_2O$ [wt%]
$SiO_2$ [wt%]

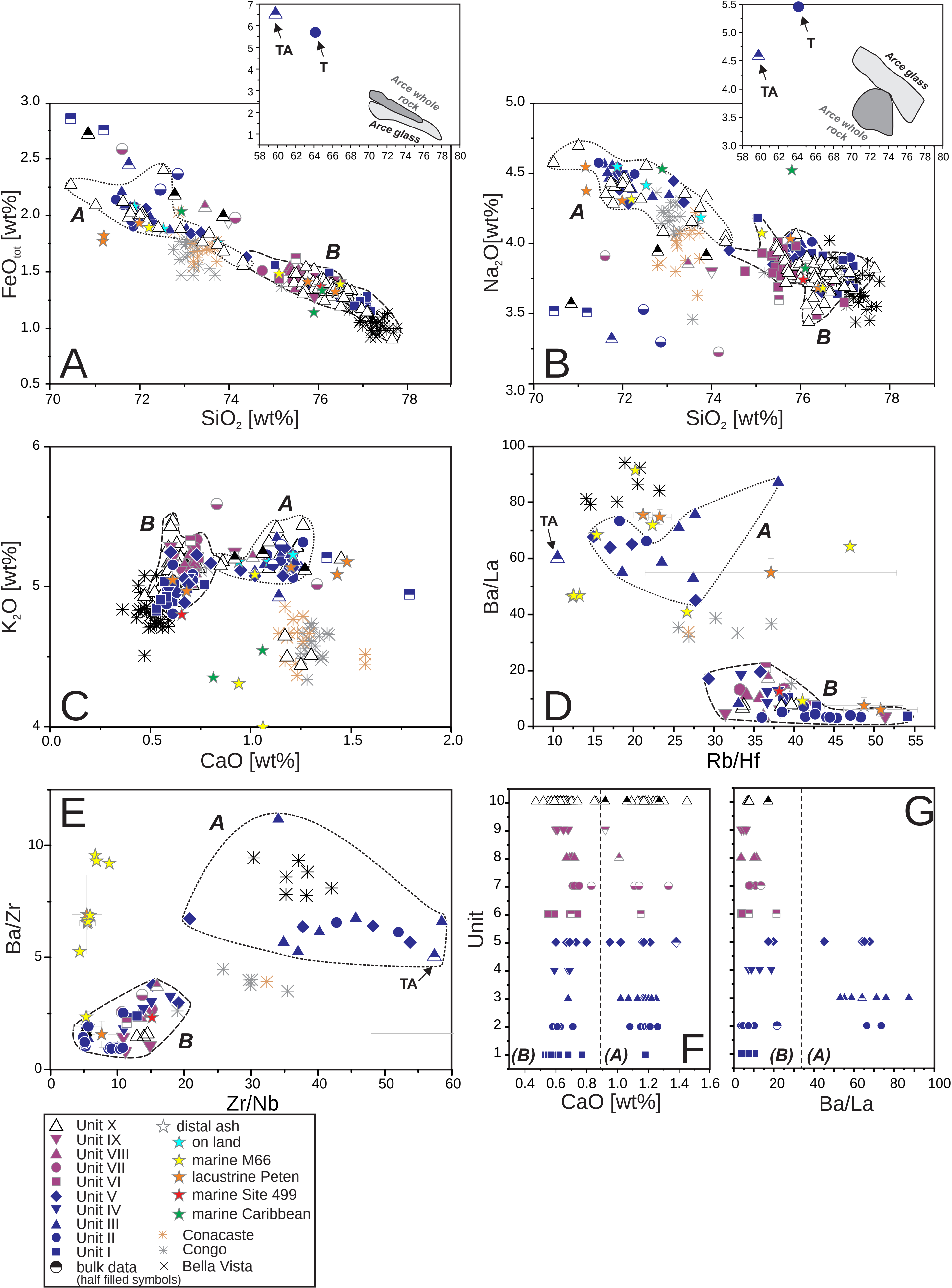
A
FeO$_{tot}$ [wt%]
SiO$_2$ [wt%]
TA
T
Arce whole rock
Arce glass
A
B
B
Na$_2$O[wt%]
SiO$_2$ [wt%]
TA
T
Arce glass
Arce whole rock
A
B
C
K$_2$O [wt%]
CaO [wt%]
A
B
D
Ba/La
Rb/Hf
TA
A
B
E
Ba/Zr
Zr/Nb
A
B
TA
F
Unit
CaO [wt%]
(B)
(A)
G
Ba/La
(B)
(A)
Unit X
Unit IX
Unit VIII
Unit VII
Unit VI
Unit V
Unit IV
Unit III
Unit II
Unit I
bulk data (half filled symbols)
distal ash
on land
marine M66
lacustrine Peten
marine Site 499
marine Caribbean
Conacaste
Congo
Bella Vista

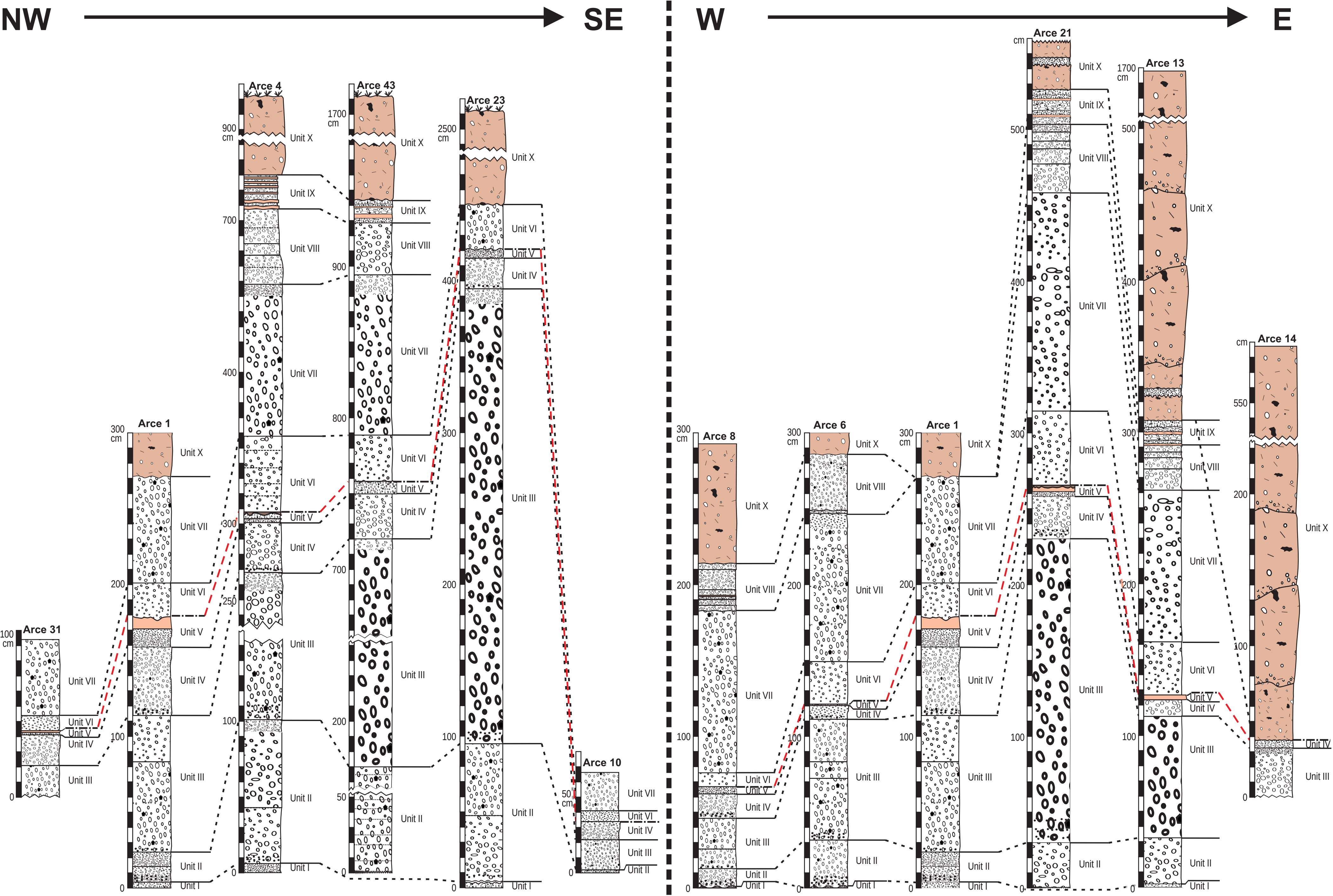
NW
SE
W
E
Arce 31
100 cm
0
Unit VII
Unit VI
Unit V
Unit IV
Unit III
Arce 1
300 cm
200
100
0
Unit X
Unit VII
Unit VI
Unit V
Unit IV
Unit III
Unit II
Unit I
Arce 4
900 cm
700
400
300
250
100
0
Unit X
Unit IX
Unit VIII
Unit VII
Unit VI
Unit V
Unit IV
Unit III
Unit II
Unit I
Arce 43
1700 cm
900
800
700
200
50
0
Unit X
Unit IX
Unit VIII
Unit VII
Unit VI
Unit V
Unit IV
Unit III
Unit II
Arce 23
2500 cm
400
300
200
100
0
Unit X
Unit VI
Unit V
Unit IV
Unit III
Unit II
Unit I
Arce 10
50 cm
0
Unit VII
Unit VI
Unit IV
Unit III
Unit II
Arce 8
300 cm
200
100
0
Unit X
Unit VIII
Unit VII
Unit VI
Unit V
Unit IV
Unit III
Unit II
Unit I
Arce 6
300 cm
200
100
0
Unit X
Unit VIII
Unit VII
Unit VI
Unit V
Unit IV
Unit III
Unit II
Unit I
Arce 1
300 cm
200
100
0
Unit X
Unit VII
Unit VI
Unit V
Unit IV
Unit III
Unit II
Unit I
Arce 21
cm
500
400
300
200
100
0
Unit X
Unit IX
Unit VIII
Unit VII
Unit VI
Unit V
Unit IV
Unit III
Unit II
Arce 13
1700 cm
500
400
300
200
100
0
Unit X
Unit IX
Unit VIII
Unit VII
Unit VI
Unit V
Unit IV
Unit III
Unit II
Unit I
Arce 14
cm
550
200
100
0
Unit X
Unit IV
Unit III


A
UACT
LACT
B
Ig
Fall
erosional unconformity
C
X
IX
VIII
VII
V+VI
IV
III
D
III
IIb
IIa
I
E
FU 3
FU 2
FU 1
F
reworked
H
UACT
LACT
PET06-1B-16H-2, 72.2-72.5 & 75.4-78 cm
72
73
74
75
76
77
78
79
80
81
I
UACT
LACT
PET06-6B-19E-2, 106.4-106.8 & 111 - 112.4 cm
107
108
109
110
111
112
113
114
115
G
III
IIb
IIa
I

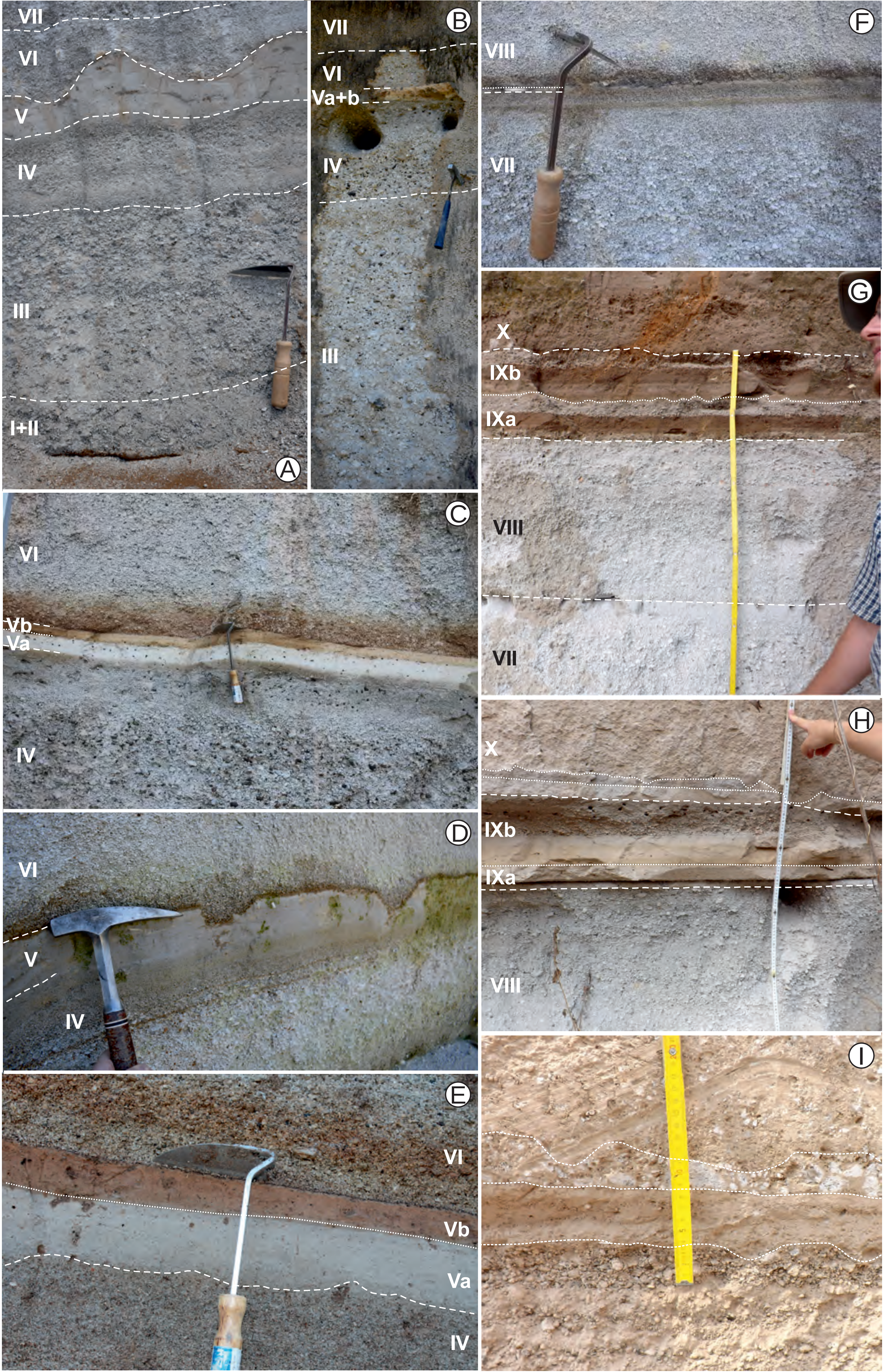
A
VII
VI
V
IV
III
I+II
B
VII
VI
Va+b
IV
III
F
VIII
VII
G
X
IXb
IXa
VIII
VII
C
VI
Vb
Va
IV
H
X
IXb
IXa
VIII
D
VI
V
IV
E
VI
Vb
Va
IV
I

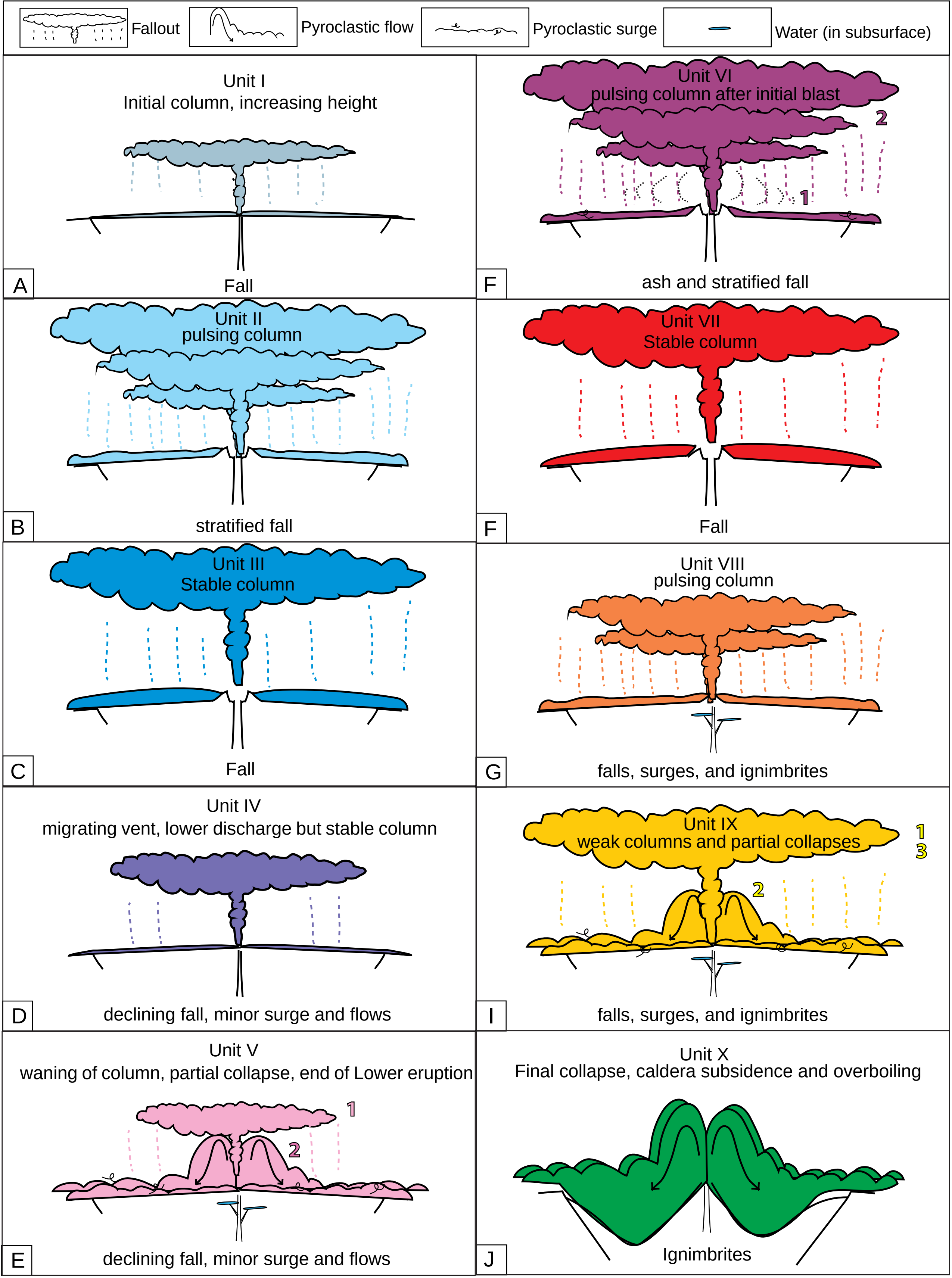
Fallout
Pyroclastic flow
Pyroclastic surge
Water (in subsurface)
Unit I
Initial column, increasing height
Fall
A
Unit VI
pulsing column after initial blast
2
1
ash and stratified fall
F
Unit II
pulsing column
stratified fall
B
Unit VII
Stable column
Fall
F
Unit III
Stable column
Fall
C
Unit VIII
pulsing column
falls, surges, and ignimbrites
G
Unit IV
migrating vent, lower discharge but stable column
declining fall, minor surge and flows
D
Unit IX
weak columns and partial collapses
1
3
2
falls, surges, and ignimbrites
I
Unit V
waning of column, partial collapse, end of Lower eruption
1
2
declining fall, minor surge and flows
E
Unit X
Final collapse, caldera subsidence and overboiling
Ignimbrites
J

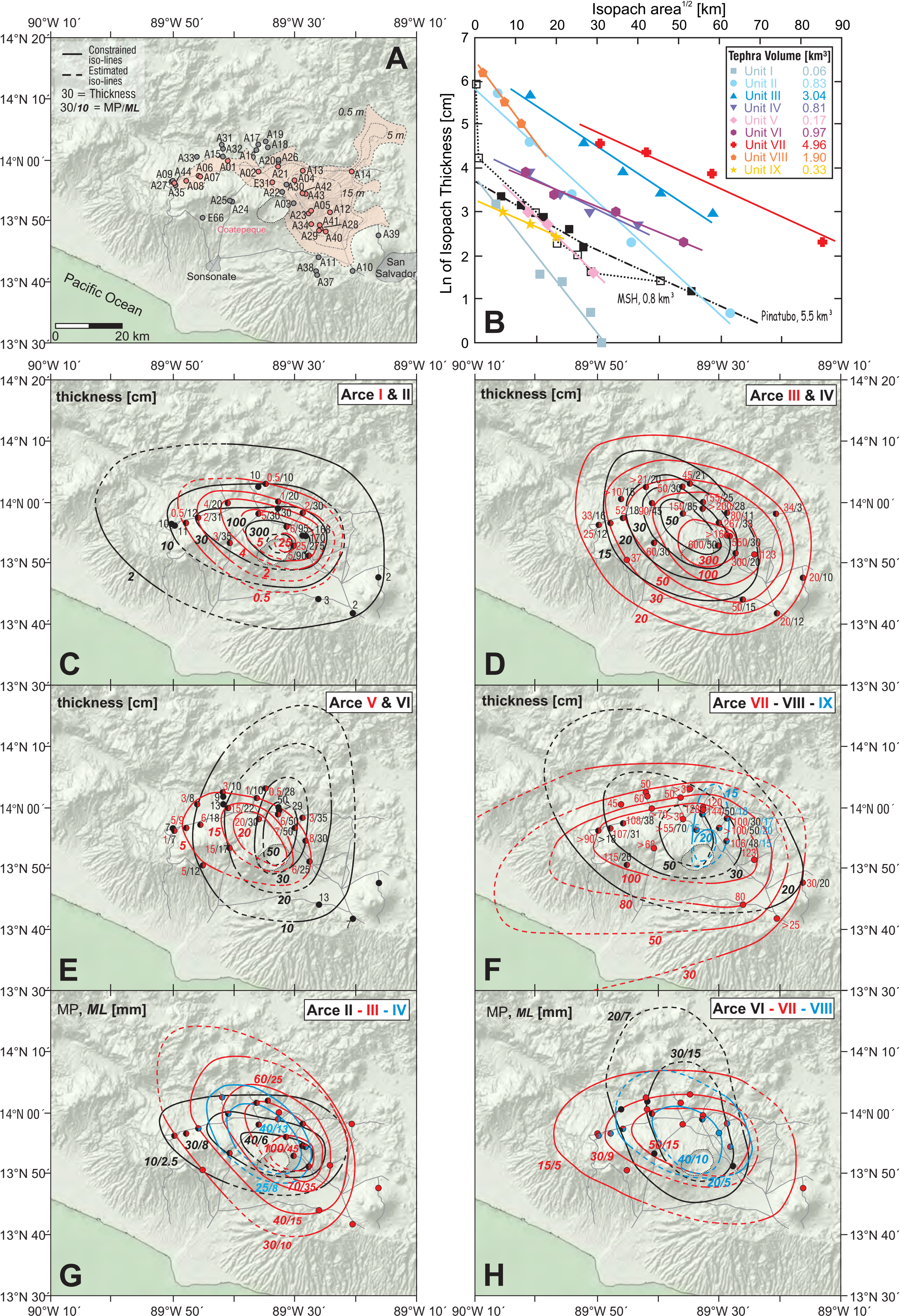
A
Constrained iso-lines
Estimated iso-lines
30 = Thickness
30/10 = MP/ML
0.5 m
5 m
15 m
Coatepeque
Sonsonate
San Salvador
Pacific Ocean
0
20 km
B
Isopach area$^{1/2}$ [km]
Ln of Isopach Thickness [cm]
Tephra Volume [km$^3$]
Unit I 0.06
Unit II 0.83
Unit III 3.04
Unit IV 0.81
Unit V 0.17
Unit VI 0.97
Unit VII 4.96
Unit VIII 1.90
Unit IX 0.33
MSH, 0.8 km$^3$
Pinatubo, 5.5 km$^3$
C
thickness [cm]
Arce I & II
D
thickness [cm]
Arce III & IV
E
thickness [cm]
Arce V & VI
F
thickness [cm]
Arce VII - VIII - IX
G
MP, ML [mm]
Arce II - III - IV
60/25
40/13
40/6
100/45
30/8
10/2.5
25/8
70/35
40/15
30/10
H
MP, ML [mm]
Arce VI - VII - VIII
20/7
30/15
50/15
40/10
30/9
15/5
20/5
90°W 10´
89°W 50´
89°W 30´
89°W 10´
14°N 20´
14°N 10´
14°N 00´
13°N 50´
13°N 40´
13°N 30´

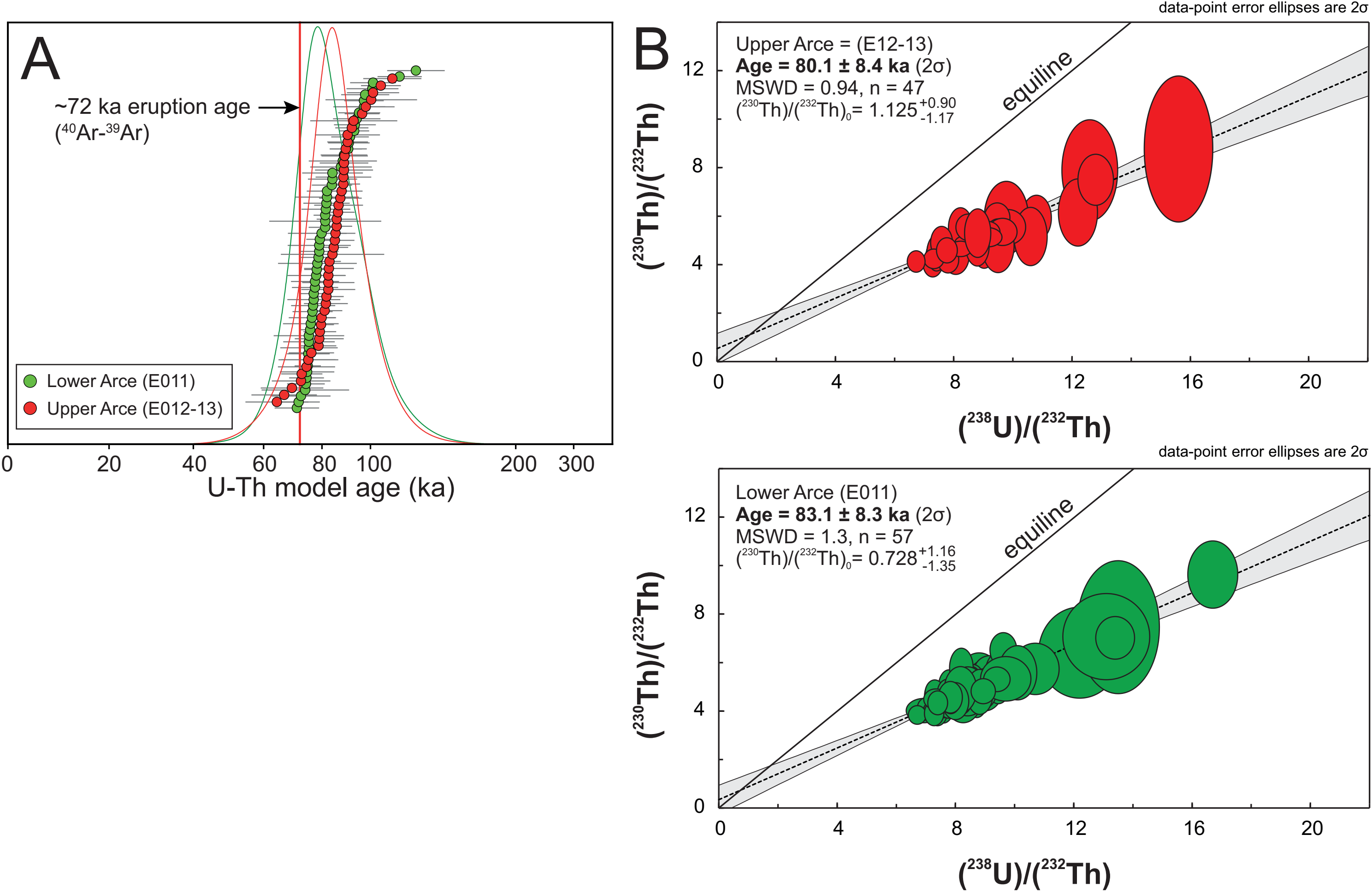
A
~72 ka eruption age
($^{40}$Ar-$^{39}$Ar)
Lower Arce (E011)
Upper Arce (E012-13)
0
20
40
60
80
100
200
300
U-Th model age (ka)
B
data-point error ellipses are 2σ
Upper Arce = (E12-13)
Age = 80.1 ± 8.4 ka (2σ)
MSWD = 0.94, n = 47
($^{230}$Th)/($^{232}$Th)$_0$= 1.125$^{+0.90}_{-1.17}$
equiline
($^{230}$Th)/($^{232}$Th)
0
4
8
12
0
4
8
12
16
20
($^{238}$U)/($^{232}$Th)
data-point error ellipses are 2σ
Lower Arce (E011)
Age = 83.1 ± 8.3 ka (2σ)
MSWD = 1.3, n = 57
($^{230}$Th)/($^{232}$Th)$_0$= 0.728$^{+1.16}_{-1.35}$
equiline
($^{230}$Th)/($^{232}$Th)
0
4
8
12
0
4
8
12
16
20
($^{238}$U)/($^{232}$Th)

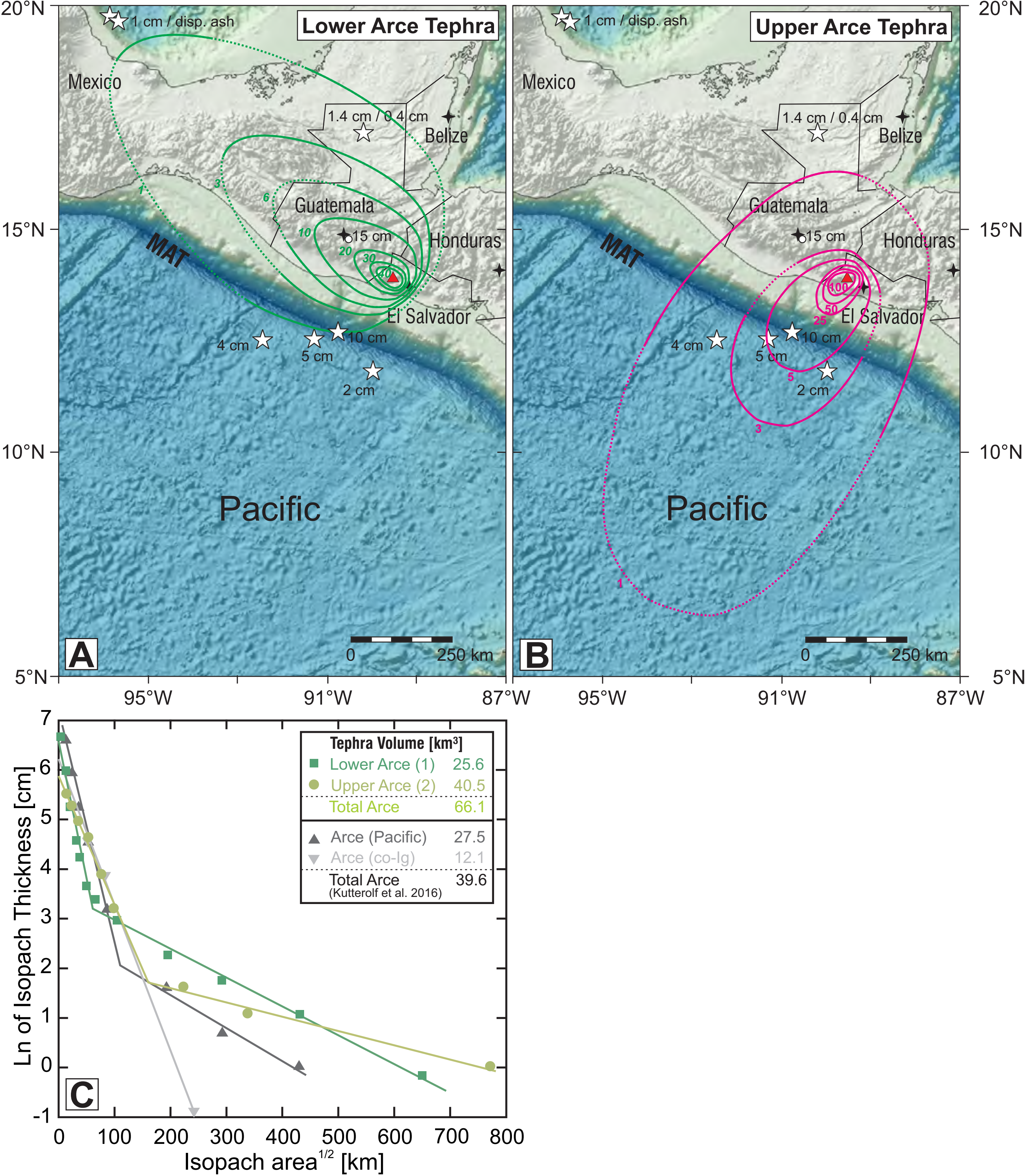
Lower Arce Tephra
Upper Arce Tephra
1 cm / disp. ash
Mexico
1.4 cm / 0.4 cm
Belize
Guatemala
15 cm
Honduras
El Salvador
MAT
4 cm
5 cm
10 cm
2 cm
Pacific
1
3
6
10
20
30
40
5
25
50
100
0
250 km
A
B
20°N
15°N
10°N
5°N
95°W
91°W
87°W
C
Ln of Isopach Thickness [cm]
Isopach area$^{1/2}$ [km]
7
6
5
4
3
2
1
0
-1
0
100
200
300
400
500
600
700
800
Tephra Volume [km³]
Lower Arce (1) 25.6
Upper Arce (2) 40.5
Total Arce 66.1
Arce (Pacific) 27.5
Arce (co-Ig) 12.1
Total Arce 39.6
(Kutterolf et al. 2016)

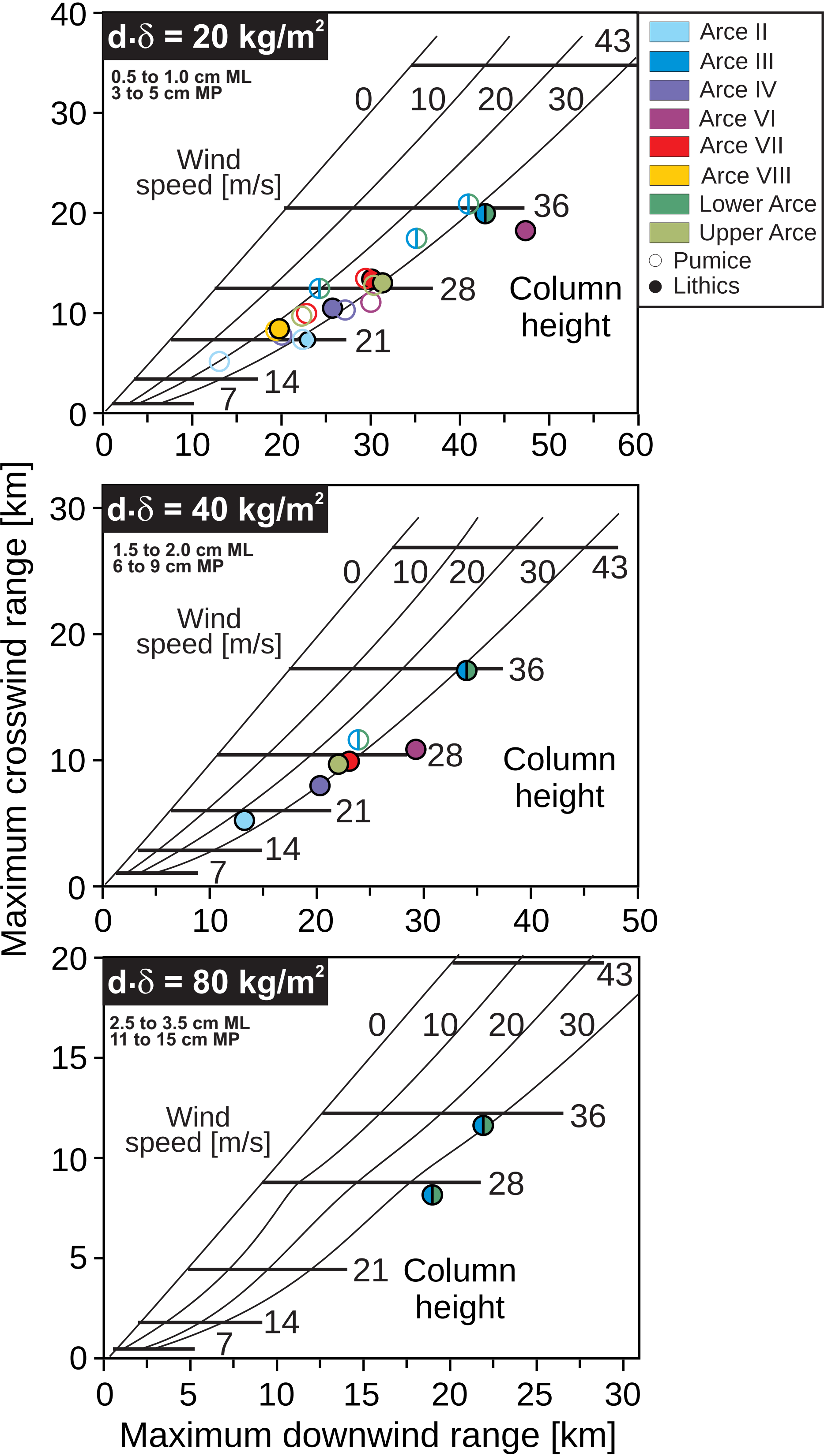
d·δ = 20 kg/m²
0.5 to 1.0 cm ML
3 to 5 cm MP
Wind speed [m/s]
0
10
20
30
43
36
28
21
14
7
Column height
Arce II
Arce III
Arce IV
Arce VI
Arce VII
Arce VIII
Lower Arce
Upper Arce
○ Pumice
● Lithics
0
10
20
30
40
0
10
20
30
40
50
60
d·δ = 40 kg/m²
1.5 to 2.0 cm ML
6 to 9 cm MP
Wind speed [m/s]
0
10
20
30
43
36
28
21
14
7
Column height
0
10
20
30
0
10
20
30
40
50
d·δ = 80 kg/m²
2.5 to 3.5 cm ML
11 to 15 cm MP
Wind speed [m/s]
0
10
20
30
43
36
28
21
14
7
Column height
0
5
10
15
20
0
5
10
15
20
25
30
Maximum crosswind range [km]
Maximum downwind range [km]

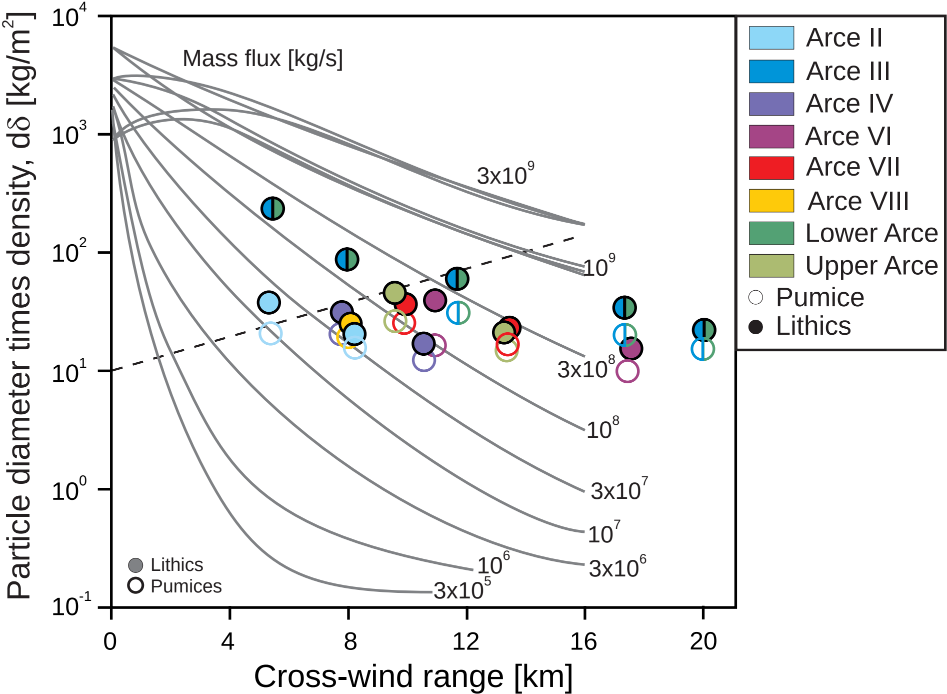
Mass flux [kg/s]
3x10^9
10^9
3x10^8
10^8
3x10^7
10^7
3x10^6
10^6
3x10^5
Lithics
Pumices
Arce II
Arce III
Arce IV
Arce VI
Arce VII
Arce VIII
Lower Arce
Upper Arce
Pumice
Lithics
Particle diameter times density, dδ [kg/m^2]
10^4
10^3
10^2
10^1
10^0
10^-1
Cross-wind range [km]
0
4
8
12
16
20

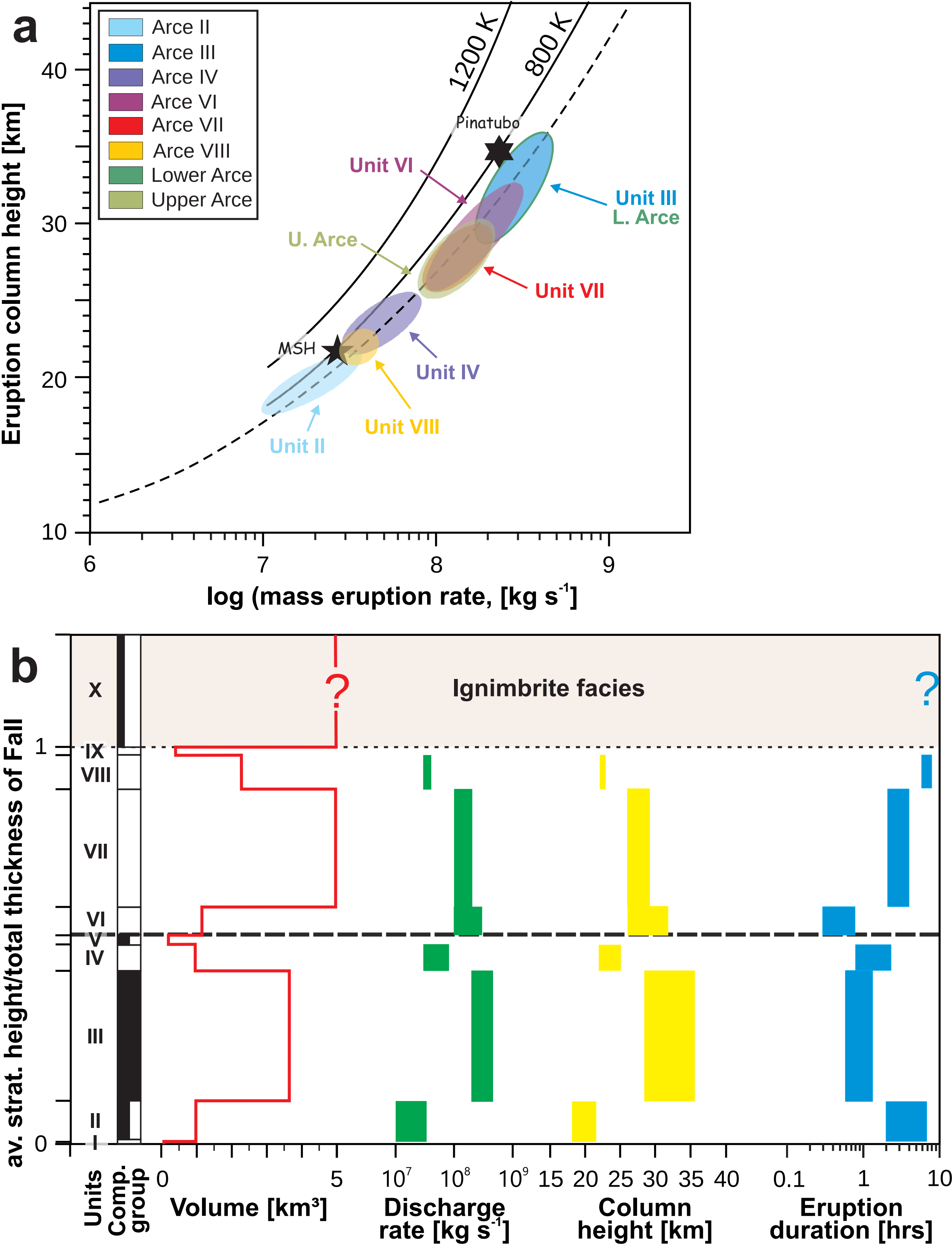
a
Arce II
Arce III
Arce IV
Arce VI
Arce VII
Arce VIII
Lower Arce
Upper Arce
1200 K
800 K
Pinatubo
MSH
Unit VI
Unit III
L. Arce
U. Arce
Unit VII
Unit IV
Unit II
Unit VIII
Eruption column height [km]
10
20
30
40
6
7
8
9
log (mass eruption rate, [kg s-1])
b
Ignimbrite facies
?
?
X
IX
VIII
VII
VI
V
IV
III
II
I
0
1
av. strat. height/total thickness of Fall
Units
Comp. group
0
5
Volume [km³]
10⁷
10⁸
10⁹
Discharge rate [kg s-1]
15
20
25
30
35
40
Column height [km]
0.1
1
10
Eruption duration [hrs]

**Table 1:** Eruption parameter for the Arce Tephra devided into individual stratigraphic units (Vp), their cumulative eruptive parameter summarized also in Lower and Upper Arce numbers and comparison to eruptive parameter (e.g. volumes; VT) determined by using integrated isolines for Upper and Lower Arce and their consideration in distal and proximal areas.

| Stratigraphic unit | minimum* distal distribution area (km$^2$) | Proximal tephra volume (km³) | Distal tephra volume (km³) | Ignimbrite tephra volume (km³) | Total tephra volume (km³) | Total DRE volume (km³) | Total erupted mass (kg) | av. Maximum eruption column height (km) | av. discharge | Eruption duration (hrs) |
|---|---|---|---|---|---|---|---|---|---|---|
| ***Indiviudual unit esitmates (VP) using only the isopachs of each unit*** | | | | | | | | | | |
| **Arce I** | **1.3x10$^3$** | 0.06 | | | 0.06 | 0.01 | 1.90E+10 | na | na | na |
| **Arce II** | **3.9x10$^3$** | 0.83 | | | 0.83 | 0.12 | 2.49E+11 | 20 | 2.40x10$^7$ | 3.7 |
| **Arce III** | **3.4x10$^3$** | 3.04 | | | 3.04 | 0.43 | 9.12E+11 | 33 | 3.30x10$^8$ | 0.9 |
| **Arce IV** | **1.6x10$^3$** | 0.81 | | | 0.81 | 0.12 | 2.43E+11 | 24 | 5.00x10$^7$ | 1.5 |
| **Arce V** | **8.3x10$^2$** | 0.17 | | | 0.17 | 0.02 | 5.12E+10 | na | na | na |
| **Arce VI** | **2.6x10$^3$** | 0.97 | | | 0.97 | 0.14 | 2.90E+11 | 28 | 2.10x10$^8$ | 0.5 |
| **Arce VII** | **7.3x10$^3$** | 4.96 | | | 4.96 | 0.71 | 1.49E+12 | 27 | 1.40x10$^8$ | 3.1 |
| **Arce VIII** | **3.2x10$^3$** | 1.90 | | | 1.90 | 0.27 | 9.12E+11 | 23 | 3.50x10$^7$ | 7.4 |
| **Arce IX** | **2.0x10$^2$** | 0.33 | | | 0.33 | 0.05 | 1.00E+11 | na | na | na |
| ***individual units Arce 1*** | | *4.9* | | | *4.9* | *0.7* | *1.47E+12* | | | *6.1* |
| ***individual units Arce 2*** | | *8.2* | | | *8.2* | *1.17* | *2.79E+12* | | | *10.6* |
| ***Total Arce individual units*** | | *13.1* | | | *13.1* | *1.87* | *4.26E+12* | | | *16.7* |
| ***Integrated estimates (VT) using total isopachs (e.g. Fig. 11)*** | | | | | | | | | | |
| **Arce 1** | **3.8x10$^5$** | **4.4 (VTp)** | **18.9 (VTd)** | | **25,6** | **12,9** | **2.71E+13** | **32** | **3.3x10$^8$** | **30.0** |
| **Arce 2** | **5.9x10$^5$** | **9.5 (VTp)** | **21.0 (VTd)** | **10.0** | **40.5** | **17,5** | **3.67E+13** | **27** | **1.5x10$^8$** | **72.0** |
| **Arce total** | | | | | **66.1** | **30,4** | **6.39E+13** | | | **102.0** |

*distribution for thinnest isopach mapped